Suppression of the Optical Linewidth and Spin Decoherence of a Quantum Spin Center in a *p-n* Diode

Denis R. Candido[1,2,†] and Michael E. Flatté[1,2,3,*]

[1] *Department of Physics and Astronomy, University of Iowa, Iowa City, Iowa 52242, USA*
[2] *Pritzker School of Molecular Engineering, University of Chicago, Chicago, Illinois 60637, USA*
[3] *Department of Applied Physics, Eindhoven University of Technology, P.O. Box 513, 5600 MB Eindhoven, Netherlands*

(Received 27 September 2020; revised 22 June 2021; accepted 15 July 2021; published 15 October 2021)

We present a quantitative theory of the suppression of the optical linewidth due to charge fluctuation noise in a *p-n* diode, recently observed by Anderson *et al.* [Science 366, 1225 (2019)]. We connect the local electric field with the voltage across the diode, allowing the identification of the defect depth from the experimental threshold voltage. Furthermore, we show that an accurate description of the decoherence of such spin centers requires a complete spin-1 formalism that yields a biexponential decoherence process, and predict how reduced charge fluctuation noise suppresses the spin center's decoherence rate.

DOI: 10.1103/PRXQuantum.2.040310

I. INTRODUCTION

The effect of the environment on the optical linewidth and spin decoherence of an optically accessible spin center is well known to be significant; a major step forward in reducing environmental effects was achieved recently by the placing of a spin center in a semiconductor *p-n* diode, wherein the effects of charge fluctuations can be suppressed [1]. Applications of entangled photon pairs to quantum information require pairs that are indistinguishable [2], and thus the use of light-emitting defects to emit entangled photon pairs requires emission whose source cannot be determined, even in principle. An optical linewidth determined by local charge fluctuations breaks this indistinguishability [3]. Considerable effort has already been devoted to optimizing such optically accessible quantum-coherent spin centers associated with defects in semiconductor crystals, including by reducing the sources of magnetic [4–16] or electrical [4–7,15–19] noise from nearby surfaces or other defects. A *p-n* diode, however, provides the possibility of dynamically removing sources of noise as well as studying the properties of noise under exceptionally controlled conditions. The interest in suppressing the optical linewidth and spin decoherence of these quantum-coherent centers stems in part from their broad applicability in quantum information sciences, including quantum sensing [4,20–23] and quantum memory [24]. Their discrete optical transitions, and their direct or indirect coupling to spin, provide an avenue to probe fundamental quantum properties, e.g., teleportation [25] and spin-photon entanglement [26,27]. These spin centers can also provide components for quantum networking, e.g., through optical means [27–30] or magnonic means [31–40]. Divacancies in SiC [15,41–45] and negatively charged nitrogen-vacancy (NV) centers [27,46,47] in diamond both provide excellent optical addressability and long-lived spin coherence [1,15,43]; however, the construction of electrical or photonic devices from SiC for quantum information is often much simpler and less expensive than that of diamond devices [48]. Conversely, defects embedded in *p-n* diodes have also demonstrated tunability of single-photon emission [49–53] and charge state switching [1,51,54] through the applied voltage bias across the diode.

Here we present a quantitative theory describing the fundamental properties of the quantum-coherent spin center in the environment of a p-n-n^+ diode (see, e.g., Ref. [1] and Fig. 1), including the response of the optical transition energy, optical linewidth, and spin coherence to the diode voltage. In a complex and nonlinear fashion, the macroscopic voltage across the device affects the local electric field (and thus the optical transition energy) as well as the fluctuating electric field both in the nearby region and in the electrical device contacts. The shift of the spin center's optical transition energies via the Stark

*michael_flatte@mailaps.org
†denisricardocandido@gmail.com

Published by the American Physical Society under the terms of the Creative Commons Attribution 4.0 International license. Further distribution of this work must maintain attribution to the author(s) and the published article's title, journal citation, and DOI.

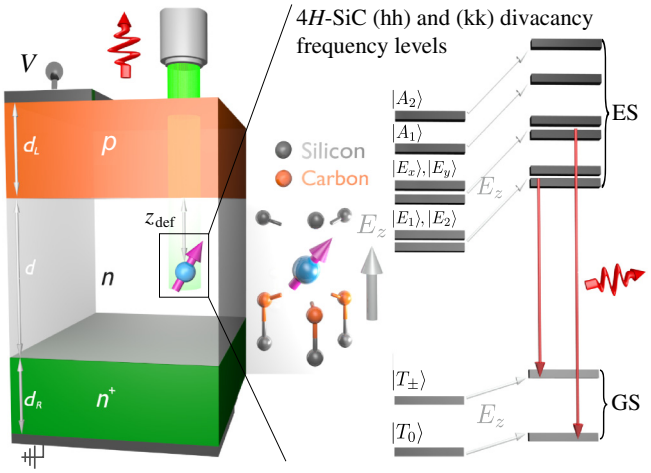

FIG. 1. The 4H-SiC p-n-n^+ diode from Ref. [1] with one divacancy located in the n region at $z = z_{\rm def}$. The (hh) or (kk) divacancy lattice configuration is shown together with the response of its frequency to an applied electric field (E_z along the defect symmetry axis) produced by the diode voltage. The red arrows represent the PL transitions addressed in this work.

effect [1,4,15,44,55–59] is expected in this configuration; however, we show a rigorous, quantitative, and analytical connection between the experimentally applied voltage and the defect's transition energy, and from that we can determine the depth of the defect within the device ($z_{\rm def}$ in Fig. 1). In Ref. [1] both the optical transition energies and the linewidths were observed via photoluminescence (PL). For new spin centers with known positions in such a diode, our results can be used to determine the local electric field, which with measured optical transition energy shifts would determine the electric dipole moments of the ground state (GS) and the excited state (ES) of the new spin center. Furthermore, we propose improved diode designs to yield shifts in the emission frequencies in response to electric fields in excess of 1 THz for 4H-SiC divacancies, while avoiding dielectric breakdown of the material.

The optical linewidth has been observed to narrow when a diode is biased to deplete nearby electrical carriers. Here our quantitative theory for the charge fluctuation noise within both the depleted regions and the nondepleted regions (the densely doped contacts) produces an analytical formula for the optical linewidth as a function of the voltage, the defect position, and the diode design (thicknesses of regions and doping densities). Although spectral diffusion due to fluctuations in the environment, which leads to a broader optical linewidth, is well known for defect emitters [60], here we describe these effects due to the unusual and tunable features of p-n diodes. The analytical calculations are confirmed by Monte Carlo simulations of the charge fluctuation noise, and reproduce accurately the experimental results of Ref. [1]. We therefore propose altered diode designs, and spin center placement within diodes, which may further reduce the optical linewidth of similar quantum-coherent spin centers. Moreover, our theory for the spectral diffusion identifies the maximum doping densities allowed that leave the linewidth close to the fundamental limit due to the optical transition lifetime, providing guidance for photonic device design, including defect emitters.

Finally, we derive an extensive theory for the ground-state spin decoherence of defects with C_{3v} point group symmetry, e.g., NV centers and (hh) and (kk) SiC divacancies. A key result is that the correct coherence times can be accurately calculated only through a spin-1 formalism including the entire defect ground-state subspace. We find a biexponential decoherence process that cannot be obtained from the spin-1/2 formalism. By considering the effect of charge fluctuation noise on the spin decoherence, we predict the consequences of the diode voltage for the quantum spin center's coherence times. We obtain analytical expressions for these coherence times as a function of the diode voltage, diode densities, temperature, the defect's position within the diode, and other sources of decoherence. This formula clarifies how the electric noise in a diode competes with other noise types, and also establishes the maximum doping densities allowed that prevent electric field noise from suppressing the spin coherence time of the emitter. These results identify a potential increase of the spin coherence time when the defect is within the depletion region, although this conclusion depends on the magnitude of the characteristic charge fluctuation time and on the ground-state dipole moment. For the diode and defect parameters from Ref. [1], no spin coherence time increase is obtained, agreeing with the experimental data. This permits the use of gated diodes to implement and manipulate defect spin qubits without susceptibility to the electric noise arising from the doped regions.

The presentation of these results in this article begins in Sec. II with the description of the GS and ES Hamiltonians for defects with C_{3v} and C_{1h} point group symmetry (electronic structure shown schematically in Fig. 1), including the coupling to an external electric field. In Sec. III we present a complete theory for the spatially dependent electric field and charge density in p-n and p-n-n^+ diodes as a function of voltage, focusing on the experimentally relevant regime of reverse voltage (charge depletion). The spin center's optical emission spectrum, including the optical linewidth calculated analytically and via numerical Monte Carlo simulation of the charge fluctuation noise, is presented in Sec. IV. Finally, in Sec. V we predict the variation of the coherence times of defects with C_{3v} symmetry as a function of diode voltage and design.

II. SPIN CENTER HAMILTONIANS

The electronic structures of defects with point group symmetries C_{3v} and C_{1h} are strongly modified by the

presence of an electric field. Examples of defects with C_{3v} point group symmetry include the negatively charged NV center in diamond [4,21,22,28,29,43,45,46,55–57,61–69] and the (hh) and (kk) divacancies in 4H-SiC [1,15,41,43–45,58,59]. Defects with C_{1h} symmetry include (hk) and (kh) divacancies in 4H-SiC [1,15,41,43–45,58,59]. The Stark effect [1,4,15,44,55–59,61] is responsible for coupling these discrete defect energy levels to the electric field. For this situation, the total GS Hamiltonian in the triplet basis $|T_-\rangle, |T_0\rangle, |T_+\rangle$ for defects with C_{3v} point group symmetry is [61,63,65,67,69]

$$\begin{aligned}\frac{\mathcal{H}_{\rm GS}^{3v}}{h} &= D_G\left(S_z^2-\frac{2}{3}\right)+d_G^{\parallel}E_z\left(S_z^2-\frac{2}{3}\right)\\ &+d_G^{\perp}E_x\left(S_y^2-S_x^2\right)+d_G^{\perp}E_y\left(S_xS_y+S_yS_x\right)\\ &+d_G'E_x\left(S_xS_z+S_zS_x\right)+d_G'E_y\left(S_yS_z+S_zS_y\right),\end{aligned} \tag{1}$$

where h is Planck's constant, D_G is the zero-energy splitting between the triplet states $m_s=0$ and $m_s=\pm1$, S_x, S_y, and S_z are the triplet spin-1 matrices, E_x, E_y, and E_z are the electric field components, and $d_G^{\parallel}$ and $d_G^{\perp}$ are electric dipole constants. For C_{3v} point group symmetry $d_G^{\parallel}\neq d_G^{\perp}$. Here the z direction corresponds to the defect symmetry axis. We emphasize that many studies have ignored the influence of the d_G' terms in Eq. (1). In the presence of small external magnetic fields, $2\gamma B_z \ll D_G$, this approximation remains valid for $d_G'\sqrt{E_x^2+E_y^2}\ll D_G$ [63,67] since in this regime these terms are responsible for the coupling between the states $|T_0\rangle$ and $|T_\pm\rangle$. From a perturbation perspective, this produces only small corrections proportional to $d_G'^2(E_x^2+E_y^2)/D_G$ in the energies of $|T_\pm\rangle$, an observation already confirmed experimentally in NV centers [63]. On the other hand, these same terms are relevant for acoustical driving of the $|T_0\rangle\leftrightarrow|T_\pm\rangle$ NV center spin transition (at large magnetic field) [70], for which $d_G'/d_G^{\perp}=\sqrt{2}(0.5\pm0.2)$ is obtained [70]. Moreover, they are also shown to be important for a correct characterization of the photoluminescence and spin dynamics near the level anticrossing in the electronic ground state [71–80]. Finally, in this work we assume $d_{G'}=0$ because (1) to the best of our knowledge there is no theoretical or experimental value for d_G' in SiC divacancies and (2) small ($2\gamma B_z\ll D_G$) magnetic fields (far from the level anticrossing in the electronic ground state) are assumed in this work. With this assumption, the eigenfrequencies of Eq. (1) are

$$\frac{E_0}{h}=-\frac{2}{3}(D_G+d_G^{\parallel}E_z), \tag{2}$$

$$\frac{E_\pm}{h}=\frac{1}{3}\left(D_G+d_G^{\parallel}E_z\right)\pm|d_G^{\perp}|\sqrt{E_x^2+E_y^2}, \tag{3}$$

where we see that E_z enters within the diagonal matrix elements, whereas E_x and E_y couple the $|T_-\rangle, |T_+\rangle$ subspace, lifting its initial degeneracy. For the ES, the Hamiltonian is [46,59,65,66]

$$\begin{aligned}\frac{\mathcal{H}_{\rm ES}^{3v}}{h} &= D_E^{\parallel}\left(S_z^2-\frac{2}{3}\right)-\lambda_E^{\parallel}\sigma_y\otimes S_z\\ &+D_E^{\perp}\left[\sigma_z\otimes\left(S_y^2-S_x^2\right)-\sigma_x\otimes\left(S_yS_x+S_xS_y\right)\right]\\ &+\lambda_E^{\perp}\left[\sigma_z\otimes\left(S_xS_z+S_zS_x\right)-\sigma_x\otimes\left(S_yS_z+S_zS_y\right)\right]\\ &+d_E^{\parallel}E_z+d_E^{\perp}\left(\sigma_zE_x-\sigma_xE_y\right),\end{aligned} \tag{4}$$

where σ_x, σ_y, and σ_z are the Pauli matrices, λ's (D_E's) are the parameters due to the spin-orbit (spin-spin) interaction, and d_E's represents the electric dipole moments. As the term $d_E^{\parallel}E_z$ enters only in the diagonal of Eq. (4), it yields a constant shift for the whole ES frequency subspace. Fig. 1 shows schematically the GS and ES discrete frequency levels and their response to an applied E_z electric field, with red arrows representing the spin-conserving optical transitions addressed in this work.

For defects with C_{1h} symmetry, e.g., (kh) or (hk) divacancies in 4H-SiC, the Hamiltonians for the ground and excited states have the same form [15]:

$$\begin{aligned}\frac{\mathcal{H}_{\rm GS(ES)}^{1h}}{h} &= D_{G(E)}^{z}\left(S_z^2-\frac{2}{3}\right)+\tilde{d}_{G(E)}^{\parallel}E_z\left(S_z^2-\frac{2}{3}\right)\\ &+D_{G(E)}^{x}\left(S_y^2-S_x^2\right)+D_{G(E)}^{y}\left(S_xS_y+S_yS_x\right),\end{aligned} \tag{5}$$

with $D_{G(E)}^{x}=\tilde{d}_{G(E)}^{\perp}E_x+D_{G(E)}^{0}$ and $D_{G(E)}^{y}=\tilde{d}_{G(E)}^{\perp}E_y+D_{G(E)}^{0}$. In contrast to the defect GS Hamiltonian with C_{3v} symmetry [Eq. (1)], here we have a lifting of the degeneracy between $m_s=\pm1$ triplet states in the absence of an electric field. This is due to the appearance of the $D_{G(E)}^{0}$ crystal field terms due to the reduced defect symmetry, yielding

$$\frac{E_{\tilde{A}_0(A_0')}}{h}=-\frac{2}{3}(D_{G(E)}^{z}+\tilde{d}_{G(E)}^{\parallel}E_z), \tag{6}$$

$$\frac{E_{\tilde{A}_\pm(A_\pm')}}{h}=\frac{1}{3}\left(D_{G(E)}^{z}+\tilde{d}_{G(E)}^{\parallel}E_z\right)\pm\sqrt{\left(D_{G(E)}^{x}\right)^2+\left(D_{G(E)}^{y}\right)^2}. \tag{7}$$

III. p-n AND p-n-n^+ DIODE ELECTRIC FIELDS AND CARRIER DENSITIES

In this work our defects are assumed to be placed or built within a p-n-n^+ diode configuration. Within the reverse-bias regime, where a negligible current passes through the

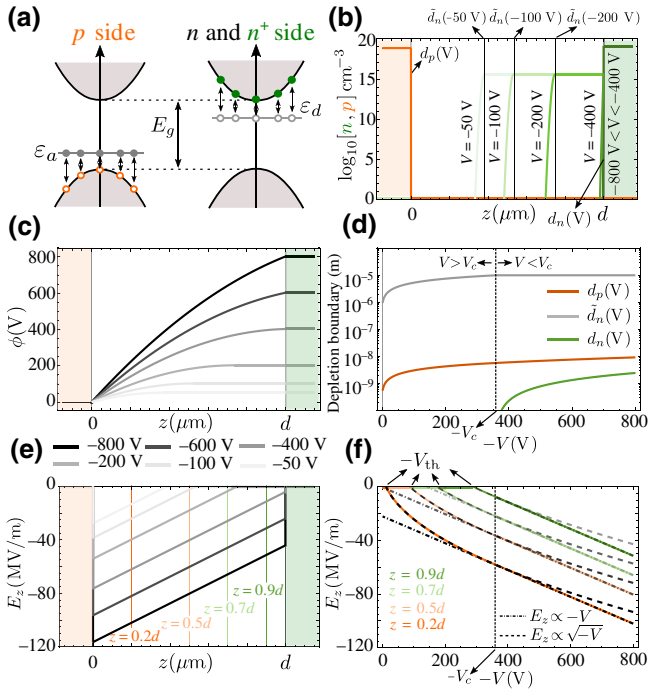

FIG. 2. (b) Electron (n) and hole (p) density carriers in the z direction for different applied reverse voltages V. (c) Electrostatic potential $\phi(z)$ along the diode for voltages V ranging from -12 to -400 V. (d) Depletion region boundary positions as a function of V. (e) Electric field profile in the z direction for voltages V ranging from -12 to -400 V. (f) Electric field as a function of V at four different positions: $z = 0.2d$, $z = 0.5d$, $z = 0.7d$, and $z = 0.9d$.

diode, the dc electric field experienced by our defect is produced by an interplay of the electric field arising from the depletion region formation and from the voltage $-V$ applied across the diode device (Fig. 1). The orange and green regions in Fig. 1 represent the p and n^+ regions, respectively, with acceptor impurity density N_A and donor impurity density N_D . The white region represents the n region, with donor density $N \ll N_D$. In the following subsections we use the theory of diodes for the reverse-bias regime to derive analytically the important quantities for the defect's optical and spin dynamical properties (e.g., carrier densities and electric field profiles). Secondly, we plot and analyze these quantities for the diode configuration in Ref. [1] under different applied voltages and at different positions.

A. Fundamental theory and key equations

Diodes usually consist of a homogeneous and neutral semiconductor with a spatially dependent doped region [Fig. 2(a)]. The semiconductor's band gap, $E_g = \epsilon_c - \epsilon_v$, where ϵ_c and ϵ_v correspond to the energy of the conduction and valence bands, respectively [Fig. 2(a)].

1. p-n diode regime

We consider first the p-n region of the p-n-n^+ diode shown in Fig. 1, and so we use N for the donor concentration in the n region ($0 < z < d$) and N_D for the donor concentration in the n^+ region ($d < z < d + d_R$). By doping the material with an acceptor impurity density N_A for $-d_L < z < 0$ (with energy $\epsilon_a \gtrsim \epsilon_v$) and a donor impurity density N in the n region $0 < z < d$ (with energy $\epsilon_d \lesssim \epsilon_c$), we obtain the p-n diode region (orange and white regions in Fig. 1). For temperatures T such that $\epsilon_c - \epsilon_d \gtrsim k_B T$ and $\epsilon_a - \epsilon_v \gtrsim k_B T$, where k_B is the Boltzmann constant, the dopants are excited and populate the conduction and valence bands with electrons and holes [Fig. 2(a)]. After ionization the carriers in the conduction and valence bands are free to move and start to recombine with each other. This recombination produces a region with few free carriers (depletion region) and a spatially dependent charged background that in turn produces an electric field in the z direction.

For the fully ionized case, we have an approximate background charge distribution $\rho(z)$ given by

$$\rho(z) = \begin{cases} 0, & z < -\tilde{d}_p(V), \\ -eN_A, & -\tilde{d}_p(V) < z < 0, \\ eN, & 0 < z < \tilde{d}_n(V) < d, \\ 0, & z > d, \end{cases} \tag{8}$$

where $e > 0$ is the fundamental electronic charge, and the positions $-\tilde{d}_p(V)$ and $\tilde{d}_n(V)$ define the spatial boundaries of the depletion region. The background charge density produces both an electrostatic potential $\phi(z)$ and an electric field $\mathbf{E} = -(\partial\phi/\partial z)\hat{z}$, obtained through the Poisson equation

$$\partial_z^2 \phi(z) = -\frac{1}{\epsilon}\rho(z), \tag{9}$$

where ϵ is the dielectric constant of our diode material. Here we assume small variations of the electrostatic potential along the x and y axis, so $\partial_x^2\phi = \partial_y^2\phi \approx 0$, and Eq. (9) follows. Using the boundary condition $\phi|_{z\to-\infty} = d\phi/dz|_{z\to-\infty} = d\phi/dz|_{z\to\infty} = 0$, we solve Eq. (9), obtaining

$$\phi(z) = \begin{cases} 0, & z < -\tilde{d}_p(V), \\ \frac{e}{2\epsilon}N_A\left[z + \tilde{d}_p(V)\right]^2, & -\tilde{d}_p(V) < z < 0, \\ \phi_\infty(V) - \frac{e}{2\epsilon}N\left[z - \tilde{d}_n(V)\right]^2, & 0 < z < \tilde{d}_n(V), \\ \phi_\infty(V), & \tilde{d}_n(V) < z, \end{cases} \tag{10}$$

with

$$\tilde{d}_n(V) = \sqrt{\frac{2\epsilon\phi_\infty(V)}{e}\frac{N_A/N}{N_A+N}} \le d, \tag{11}$$

$$\tilde{d}_p(V) = \frac{N}{N_A}\tilde{d}_n(V). \tag{12}$$

Here $\phi_\infty(V) = (1/e)\left\{E_g + k_BT\ln\left[N_DN_A/N_c(T)P_v(T)\right] - eV\right\}$ is obtained by our fixing a constant chemical potential μ along the entire sample, with $N_c(T) = \frac{1}{4}\left(2m_ck_BT/\pi\hbar^2\right)^{3/2}$ and $P_v(T) = \frac{1}{4}\left(2m_vk_BT/\pi\hbar^2\right)^{3/2}$, and effective conduction and valence band masses, m_c and m_v, respectively. The electric field is straightforwardly obtained from Eq. (10):

$$E_z(z,V) = \begin{cases} 0, & z < -\tilde{d}_p(V), \\ -\frac{e}{\epsilon}N_A\left[z+\tilde{d}_p(V)\right], & -\tilde{d}_p(V) < z < 0, \\ \frac{e}{\epsilon}N\left[z-\tilde{d}_n(V)\right], & 0 < z < \tilde{d}_n(V), \\ 0, & \tilde{d}_n(V) < z < d. \end{cases} \tag{13}$$

To obtain Eq. (13) we assume the voltage drops only inside the depletion region, so the electric field vanishes outside. Finally, the majority carrier densities of electrons and holes can be expressed as a function of the position z and the voltage V as

$$n_c(z,V) = \begin{cases} 0, & z < 0, \\ Ne^{-e[\phi_\infty(V)-\phi(z)]/k_BT}, & 0 < z < d, \\ N_De^{-e[\phi_\infty(V)-\phi(z)]/k_BT}, & z > d \end{cases} \tag{14}$$

and

$$p_v(z,V) = \begin{cases} N_Ae^{e\phi(z)/k_BT}, & z < 0, \\ 0, & 0 < z < d, \\ 0, & z > d. \end{cases} \tag{15}$$

Here we have ignored the minor carrier contributions of approximately n_c^2/N_D and approximately p_v^2/N_A as they are much smaller than the majority carrier contributions [Eqs. (14) and (15)]. Hence, we do not expect them to have a major influence on our results.

2. p-n-n$^+$ diode regime

For the critical voltage V_c, defined through $\tilde{d}_n(V_c) = d$ [Eq. (11)], with solution

$$V_c = -\frac{ed^2}{2\epsilon}\frac{N(N_A+N)}{N_A} + E_g + k_BT\ln\left(\frac{N_AN_D}{N_c(T)P_v(T)}\right), \tag{16}$$

we achieve full depletion of the n region. Therefore, for $V < V_c$ the corresponding equations [Eqs. (8) and (10)–(13)] for the effective p-n diode do not hold and must be replaced by the corresponding equations for the p-n-n^+ diode. For this situation, the background charge density is given by

$$\rho(z) = \begin{cases} 0, & z < -d_p(V), \\ -eN_A, & -d_p(V) < z < 0, \\ eN, & 0 < z < d, \\ eN_D, & d < z < d + d_n(V), \\ 0, & z > d + d_n(V), \end{cases} \tag{17}$$

where the positions $-d_p$ and d_n define the new spatial boundaries of the depletion region and read

$$d_p(V) = d\frac{N-N_D}{N_A+N_D} + \sqrt{\frac{N_D}{N_A}\frac{2\epsilon\phi_\infty(V)}{2(N_A+N_D)} + d^2\frac{N_D}{N_A}\frac{(N_D-N)(N_A+N)}{(N_A+N_D)^2}}, \tag{18}$$

$$d_n(V) = -d\frac{N+N_A}{N_A+N_D} + \sqrt{\frac{N_A}{N_D}\frac{2\epsilon\phi_\infty(V)}{e(N_A+N_D)} + d^2\frac{N_A}{N_D}\frac{(N_D-N)(N_A+N)}{(N_A+N_D)^2}}. \tag{19}$$

The electrostatic potential is obtained through Poisson's equation [Eq. (9)], yielding

$$\phi(z) = \begin{cases} 0, & z < -d_p(V), \\ \frac{e}{2\epsilon} N_A \left[z + d_p(V)\right]^2, & -d_p(V) < z < 0, \\ \frac{eN_A}{\epsilon}\left(\frac{d_p^2(V)}{2} + d_p(V)\, x\right) - \frac{eN}{2\epsilon} z^2, & 0 < z < d, \\ \phi_\infty(V) - \frac{e}{2\epsilon} N_D \left[z - d_n(V)\right]^2, & d < z < d + d_n(V), \\ \phi_\infty(V), & z > d + d_n(V). \end{cases} \tag{20}$$

The electric field within our diode is straightforwardly determined:

$$E_z(z, V) = \begin{cases} 0, & z < -d_p(V), \\ -\frac{e}{\epsilon} N_A \left[z + d_p(V)\right], & -d_p(V) < z < 0, \\ -\frac{e}{\epsilon} N_A d_p(V) + \frac{e}{\epsilon} Nz, & 0 < z < d, \\ \frac{e}{\epsilon} N_D \left[z - d_n(V)\right], & d < z < d + d_n(V), \\ 0, & z > d + d_n(V). \end{cases} \tag{21}$$

B. Results for various diode configurations

As mentioned earlier, the idea of this work is to use the diode setup to manipulate and control the defect PL linewidth and frequencies and the coherence time of our defect. A good setup is achieved by setting $N \ll N_A \lesssim N_D$ with $d \gg d_L$, which leads to a small charge concentration within a large spatial region and a large electric field within the N region. To simulate a realistic system, we use in this work the following diode parameters from Ref. [1], which considers divacancies within a 4H-SiC p-n-n^+ diode: $N_A = 7 \times 10^{18}$ cm^{-3}, $N \approx 4 \times 10^{15}$ cm^{-3}, $N_D = 10 \times 10^{18}$ cm^{-3}, $d_R \gg d = 10$ μm, $d_L = 400$ nm, $\epsilon = 9.6\epsilon_0$, and $T \approx 10$ K. Although the results here are presented for the particular case of a 4H-SiC diode, the same would hold for any diode material with alterations in the material parameters if the donors and acceptors have shallow states. Some materials, such as diamond, do not possess both shallow donors and acceptors, and so the expressions here would be considerably more complicated to account for incomplete dopant ionization.

All the results for the corresponding diode quantities are given in Fig. 2. In Fig. 2(b) we plot the density of free carriers [Eqs. (14) and (15)] for different voltages within the reverse-bias regime, which shows that the larger the modulus of V, the more we deplete the charge carriers. The spatial boundary positions of the depletion region are plotted in Fig. 2(d), which also captures the increase of the depleted region size as a function of the voltage. Moreover, for $|V| > |V_c|$, the n region becomes 100% depleted and $\tilde{d}_n(V)$ becomes a constant with value d. In both Figs. 2(d) and 2(f) we indicate the critical voltage $V_c \approx -(ed^2/2\epsilon)[N(N_A + N)/N_A] \approx -373$ V, at which the system stops behaving as an effective p-n diode and starts behaving as a p-n-n^+ diode. Figure 2(c) shows the electrostatic potential profile along the z axis for different voltages spanning from -50 to -800 V. In Fig. 2(e) we plot the electric field profile in the diode for different voltages in the reverse-bias regime. The electric field shows a linear trend with respect to the position until we reach the outside of the depletion region, where the electric field becomes zero. The linear trend in the slope is easily understood through the integration of Gauss's equation [Eq. (13)] $\partial_z E_z(z) = -\rho(z)/\epsilon \rightarrow E_z(z) \propto eNz/\epsilon$, while the amplitude of the electric field is proportional to the voltage drop V/d. In Fig. 2(f) we plot the local electric field at positions $z = 0.2d$, $0.5d$, $0.7d$, and $0.9d$ as a function of the applied voltage V. For large absolute values of V, a linear trend with respect to V is observed for most of the voltage region, and is understood through $E_z \approx V/d$ [dashed-dotted line in Fig. 2(f)]. However, we also observe a nonlinear trend for $|V| < |V_c|$. To understand this we have to recall that for these voltages the n region is not fully depleted, and its depletion region length depends on V approximately as $\sqrt{-2\epsilon V/eN}$ [Eq. (11)], thus yielding a nonlinear dependence of the electric field with respect to V given by $-(e/\epsilon)N\left(z - \sqrt{-2\epsilon V/eN}\right)$ [dashed line in Fig. 2(f)]. Therefore, we understand that this nonlinear trend of E_z versus V is a peculiarity of a p-n-n^+ diode becoming an effective p-n diode. It is important to mention that the depletion region sizes in the both p region and the n^+ region, $d_p(V)$ and $d_n(V)$, also have a $\sqrt{-V}$ dependence as can be seen from Eqs. (18) and (19) and in Fig. 2(d). Therefore, in principle even for $|V| > |V_c|$ we would expect an electric field deviating from the linear trend. However, because of the large electronic density of both the p region and the n^+ region, $N_D, N_A \gg N$, we find $d_p(V), d_n(V) \ll d$, and hence we can assume the voltage drop V happens only within the n region with

length d, thus yielding $E_z \approx V/d$. Finally, the electric field at the fixed positions $z = 0.2d$, $0.5d$, $0.7d$, and $0.9d$ in Fig. 2(f) approaches zero at the threshold voltages $V_{\rm th}$, for which these positions match the depletion boundary, i.e., $\tilde{d}_n(V_{\rm th}) = z$, thus experiencing no electric field. Through this observation we can determine the defect's position along the z axis, $z_{\rm def}$, by accessing only the experimental $V_{\rm th}$ value obtained from PL measurements. More specifically, when the defect is inside the depletion region, the shift of the PL frequency as a function of the voltage can be seen experimentally. However, when we tune $V = V_{\rm th}$, the PL frequency stops responding to the applied voltage as the defect is now outside the depletion region. This condition happens for

$$z_{\rm def}(V_{\rm th}) = \sqrt{\frac{2\epsilon}{e}\frac{N_A/N}{N_A+N}\phi_\infty(V_{\rm th})}, \tag{22}$$

and it allows the precise determination of the spin center's position within the diode. Finally, the different electric field trends as a function of the voltage are important because they establish the relation between the experimental applied voltage and the electric field felt by a defect located at $0 < z_{\rm def} < d$. We summarize these trends using Eqs. (11)–(13) and (21), with $N_A, N_D \gg N$ and $eV \gg E_g, k_B T$:

$$E_z(z_{\rm def}, V) \approx \begin{cases} 0, & |V| < |V_{\rm th}|, \\ -\dfrac{e}{\epsilon}N\left(z_{\rm def} - \sqrt{-\dfrac{2\epsilon V N_A/N}{e(N_A+N)}}\right), & |V_{\rm th}| < V < |V_c|, \\ -\dfrac{e}{\epsilon}N\left(z_{\rm def} - \dfrac{d}{2}\right) + \dfrac{V}{d}, & |V| > |V_c|. \end{cases} \tag{23}$$

IV. DEFECT EMISSION SPECTRUM

In this section we establish and explore the relation between the defect optical emission spectrum (which can be measured, e.g., through photoluminescence) and the applied voltage across the diode. More specifically, we show analytically how the frequency and the linewidth of the defect PL depend on the reverse-bias voltages, thus obtaining a detailed theoretical description of the spectral diffusion of the defect's emission. We also provide different schemes for the diode configurations and defect's position that yield terahertz shifts in the PL. Moreover, we compare our predictions with experimental data from Ref. [1], and good agreement is seen.

A. Stark shift

First, we assume the spin center is located at $\mathbf{r}_{\rm def} = (x_{\rm def}, y_{\rm def}, z_{\rm def})$. From the Hamiltonians in Eqs. (1), (4), and (5), we then obtain the defect transition frequencies as a function of the electric field. For the purpose of this work, we report the results corresponding to the PL of (hh), (kk), and (kh) 4H-SiC divacancies, which were experimentally addressed in Ref. [1]. They correspond to the $|E_y\rangle \to |T_0\rangle$ and $|E_{1,2}\rangle \to |T_\pm\rangle$ transitions for the (hh) and (kk) divacancies (Fig. 1) and the $|A_0'\rangle \to |\tilde{A}_0\rangle$ transition for the (kh) divacancy, reading

$$\Delta f^{3v}_{E_y \to T_0} = \left(d_E^{\parallel} + \frac{2}{3}d_G^{\parallel}\right) E_z(z_{\rm def}, V), \tag{24}$$

$$\Delta f^{3v}_{E_{1,2} \to T_\pm} = \left(d_E^{\parallel} - \frac{1}{3}d_G^{\parallel}\right) E_z(z_{\rm def}, V), \tag{25}$$

$$\Delta f^{1h}_{A_0' \to \tilde{A}_0} = -\frac{2}{3}\left(\tilde{d}_E^{\parallel} - \tilde{d}_G^{\parallel}\right)\cos(109.5^\circ) E_z(z_{\rm def}, V), \tag{26}$$

where $E_z(z_{\rm def}, V)$ is the electric field at $z_{\rm def}$ for voltage V [Eq. (23)] and $\cos(109.5^\circ)$ accounts for the decomposition of the electric field along the high-symmetry axis of the (kh) divacancy. Although there have been many studies of the Stark effect in defects [1,4,15,44,55–59], most of these involved unipolar materials without significant charge depletion. None of them provided a quantitative relation between the voltage applied to a p-n diode and the electric field experienced by the defect, which in turn is the microscopic quantity coupled to their energy levels. Here we obtain this relation [Eq. (23)] by solving Poisson's equation [Eq. (9)] for both p-n and p-n-n^+ diodes. Most importantly, through Eqs. (23)–(26) we are able to understand the quantitative dependence of defect frequency shift on the voltage and the diode parameters. For instance, we are able to predict that as the n region's doping density N increases, the electric field at the defect also increases, which produces shifts to higher-frequency PL. Through this connection, it is possible to engineer better diodes to achieve higher frequency shifts using smaller voltages, which becomes important as the possible applied voltages reach limits determined by the dielectric breakdown field of the material.

Because of the different dependence on the dipoles $d_G^{\parallel}$ and $d_E^{\parallel}$ of Eqs. (24) and (25), it is also possible to determine both of the spin center dipole values from experimental measurements. Usually experimental measurements [1,4,15,44,55–59] report only the values of the effective dipole moments corresponding to the addressed PL transitions. Here we provide equations that, in principle, would allow the extraction of both the $d_G^{\parallel}$ dipole moment and the $d_E^{\parallel}$ dipole moment. Through the experimental voltage dependence of the $|E_{x,y}\rangle \to |T_0\rangle$ and $|E_{1,2}\rangle \to |T_{\pm}\rangle$ transitions, we obtain from Eqs. (23)–(25) the experimental values for $d_G^{\parallel}$ and $d_E^{\parallel}$. Moreover, regarding the experimental work in Ref. [1], we observe $\Delta f_{E_y \to T_0} \approx \Delta f_{E_{1,2} \to T_{\pm}}$, which results in $d_E^{\parallel} \gg d_G^{\parallel}$, thus showing that the dipole of the excited-state manifold is the major property responsible for the Stark shift.

In Fig. 3(a) we use Eqs. (23)–(26) to fit the experimental data from Ref. [1], which contains the frequency shifts of the (hh) and (kk) $|E_y\rangle \to |T_0\rangle$ and $|E_{1,2}\rangle \to |T_{\pm}\rangle$ transitions and the (kh) $|A_0'\rangle \to |\tilde{A}_0\rangle$ transition. We fit them assuming $d_G^{\parallel} = 0$, as justified before. The frequency shifts in Fig. 3(a) have two different trends with respect to the voltages. For small voltage modulation, $|V| < |V_c|$, the frequencies have a nonlinear dependence on V, which was explained in Sec. III B as resulting from the incomplete depletion of the n region. Specifically, if the n region is not completely depleted, the depletion length depends on the voltage as $\sqrt{-V}$ [Eq. (11)], thus yielding a frequency shift proportional to $E_z \approx -V/\sqrt{-V} \approx \sqrt{-V}$. For voltage modulation larger than $|V| > |V_c|$, the n region becomes fully depleted and a frequency shift proportional to $E_z \approx -V/d$ is expected, assuming the small depletion region extends into the p and n^+ regions discussed previously. For the donor and acceptor density values reported in Ref. [1], we obtain $V_c \approx -90$ V, which is not supported by the long nonlinear trend within the 0 V $\lesssim |V| \lesssim$ 350 V range of the experimental data [Fig. 3(a)]. This suggests a larger unintentional doping density than the reported $N \approx 1 \times 10^{15}$ cm^{-3} [1]. The best fit to the experimental data is presented in Fig. 3(a), where we assume $N = 4 \times 10^{15}$ cm^{-3}. For this density, we obtain $d_{E,kk}^{\parallel} = 4.95$ GHz/MV m, $d_{E,hh}^{\parallel} = 12.75$ GHz/MV m, and $\tilde{d}_{E,kh}^{\parallel} - \tilde{d}_{G,kh}^{\parallel} = 118.07$ GHz/MV m. The dipole values obtained here agree with those in Refs. [1,44]. The apparent discrepancy regarding the (hk) dipole value [reported as 35 GHz/MV m in Ref. [1]] is because the authors incorporated the $(2/3)\cos(109.5°)$ factor in the dipole definition. By including this factor, and also taking into account the 4° off-axis nature of the diode growth [1], we obtain approximately 31.38 GHz/MV m. Furthermore, using Eq. (22), we are also able to determine the positions of spin centers along the z axis by accessing the threshold voltages V_{th}, yielding $z_{\text{def}}^{kk} = 4.42$ μm, $z_{\text{def}}^{hh} = 1.32$ μm, and $z_{\text{def}}^{kh} = 3.53$ μm. For completeness, in Appendix B we also provide the data fit using densities $N = 1 \times 10^{15}$, 2×10^{15}, and 3×10^{15} cm^{-3}, which clearly shows worse agreement.

In Figs. 3(b)–3(d) we plot the frequency shift for the (hh) divacancy $|E_y\rangle \to |T_0\rangle$ transition as a function of the voltage V and the density of the n region, N. We chose three different combinations of n region length and defect position: $d = 10$ μm with $z_{\text{def}} = 5$ μm [Fig. 3(b)], $d = 5$ μm with $z_{\text{def}} = 2.5$ μm [Fig. 3(c)], and $d = 2$ μm with $z_{\text{def}} = 1$ μm [Fig. 3(d)]. In all three configurations we are able to obtain an (hh) frequency shift greater than 1 THz under operable voltages. However, as $E_z \approx V/d$, the smaller the length d, the smaller the applied voltage to observe terahertz shifts. For the situation in Fig. 3(d), we obtain terahertz shifts even with small applied voltages $V \approx -200$ V. As we discuss below, the only drawback of having diodes with small length d is that the defect becomes closer to the nondepleted p and n^+ regions, thus being more sensitive to the electric noise caused by the

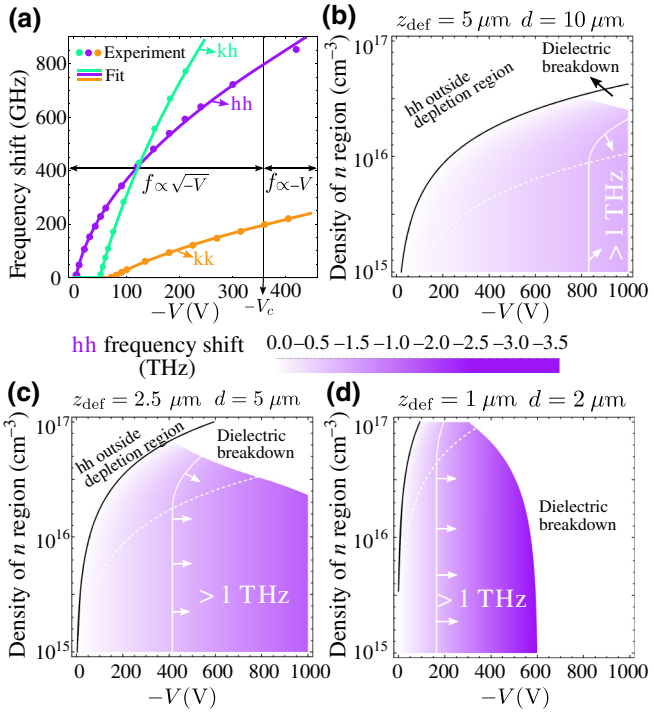

FIG. 3. (a) Fit for the frequency shift versus voltage V for the $|E_y\rangle \to |T_0\rangle$ and $|E_{1,2}\rangle \to |T_{\pm}\rangle$ (hh) and (kk) transitions and for the $|A_0'\rangle \to |\tilde{A}_0\rangle$ (kh) transition assuming $N = 4 \times 10^{15}$ cm^{-3}. Frequency shift of the (hh) defect as a function of the voltage and density of the n region for (b) $z_{\text{def}} = d/2 = 5$ μm, (c) $z_{\text{def}} = d/2 = 2.5$ μm, and (d) $z_{\text{def}} = d/2 = 1$ μm. The black line delimits the parameter region in which the defect is placed inside and outside the depletion region. The solid white line represents a 1-THz frequency shift, and the dashed white line represents the change from p-n to p-n-n^+ diode behavior.

fluctuation of the electric charges. In Figs. 3(b)–3(d), the black lines separate the parameter space regions in which the defect is inside and outside the depletion region. The solid white lines delimit the parameter region where we have frequency shifts greater than 1 THz, and the dashed white lines represent the parameter space region where our effective p-n diode becomes a p-n-n^+ diode. Finally, the blank regions in the right upper part represent an inaccessible parameter space region for SiC, as the field exceeds the dielectric breakdown, $E_z > -400$ MV/m.

B. Theory of the fluctuating electric field

In addition to the static dc electric field $\mathbf{E}(z_{\rm def}, V) = [0, 0, E_z(z_{\rm def}, V)]$ [Eq. (23)] that leads to the shift of the defect frequency levels and optical transition energies, we also need to take into account the temporally fluctuating electric field $\delta\mathbf{E}(t)$ that makes the frequency levels fluctuate around the average frequency values dictated by $\mathbf{E}(z_{\rm def}, V)$. These fluctuations of the frequency levels produce a finite linewidth of the PL, an effect known as spectral diffusion. For the fully ionized case of donors and acceptors, quasiuniform electron and hole gases form due to the minimization of the Coulomb energy. This quasiuniformity arises from various factors, e.g., uncertainty of particles' positions (Heisenberg uncertainty principle), thermal fluctuation of electrons' and holes' positions, and collision between different electrons (holes). In addition, because of thermal fluctuations, electrons (holes) can change from being free in the uniform gas to becoming trapped on the donor (or acceptor) atoms, which is illustrated in Fig. 4(a). Although one could argue that these thermal fluctuations are not large for the $T \approx 10$ K of Ref. [1], the laser illumination used to address the defect PL raises the electronic temperature, thus making the thermal fluctuation a potential contributor to the fluctuating charge dynamics. We consider these effects by expressing the effective coupling of a general ground (excited) state level to the total (time-dependent) electric field $\mathbf{E}(z_{\rm def}, V, t) = \mathbf{E}(z_{\rm def}, V) + \delta\mathbf{E}(t)$:

$$\frac{\mathcal{H}_{G(E)}}{h} = f_{G(E)} + \mathbf{d}^{\rm eff}_{G(E)} \cdot [\mathbf{E}(z_{\rm def}, V) + \delta\mathbf{E}(t)]. \qquad (27)$$

Although a complete description of the quasiuniform electron and hole gases is in principle a correlated many-body problem, we treat the electrons and holes as particles that do not interact with each other because of their average separation $l \approx n^{-1/3} \approx 46$ nm for typical diode n carrier densities of 10^{16} cm^{-3}. More specifically, in this work we develop a theory for the fluctuating electric field $\delta\mathbf{E}(t)$ using the physical process described in Fig. 4. We solve this problem analytically, deriving closed-form expressions for the fluctuating electric field as a function of the diode densities, diode dimensions, and spin center's position. Furthermore, we see that these results agree very well

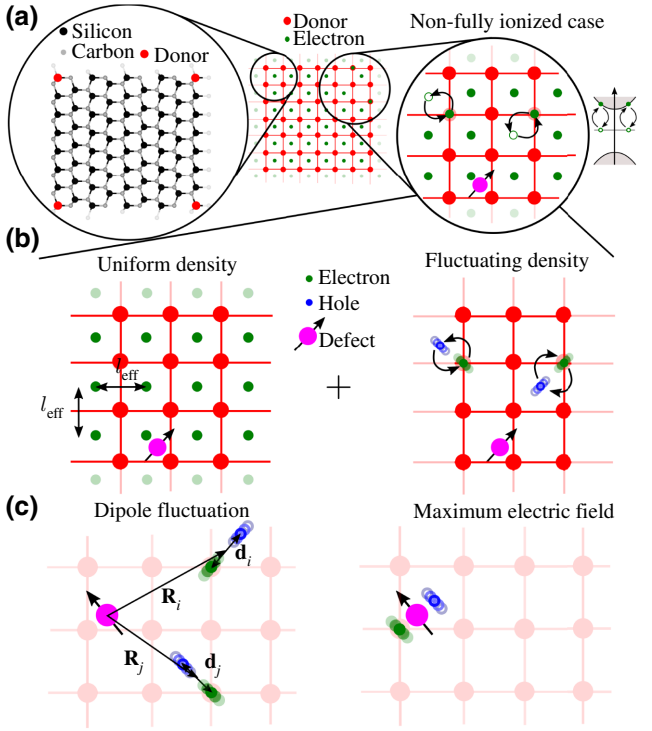

FIG. 4. (a) The 4H-SiC crystal structure with donors together with the non-fully-ionized case with fluctuation of trapped charges. (b) The total electronic density is understood as being the sum of a uniform density and a fluctuating density of electron-hole dipole pairs. (c) We model the electron-hole pair fluctuating density though the dipole approximation, where the case of maximum fluctuating electric field is shown.

with the experimental PL data from Ref. [1] and the numerical results from a Monte Carlo simulation, where we fix the donors' positions and build an electric field histogram by randomly changing the electronic positions.

C. Analytical calculation for the fluctuating electric field

Figure 4 describes the electronic structure of a semiconductor doped with donors to illustrate the origins of the fluctuating field. The schematically indicated system is 4H-SiC; however, the general approach is applicable to other semiconductor hosts. Carriers may not be fully ionized from the dopant atoms, and depending on the ionization fraction and other material parameters will produce a spatially fluctuating charge that we model here. As the positions of the charge fluctuations in Fig. 4 are random, we assume that all three components of the total electric field follow a Gaussian distribution and will produce a linewidth Γ of any specific optical transition. We consider optical emission associated with a transition from the ES to the GS (Fig. 1) for a spin center at $z_{\rm def}$; the probability function $P(f)$ of emission of a photon with frequency f is

then

$$P(f, z_{\rm def}, V) = \frac{1}{(2\pi)^{1/2}\Gamma} e^{-[f-\bar{f}(z_{\rm def},V)]^2/2\Gamma^2}, \tag{28}$$

with frequency emission peaking at

$$\bar{f}(z_{\rm def}, V) = f_E - f_G + \left(\mathbf{d}_E^{\rm eff} - \mathbf{d}_G^{\rm eff}\right)\cdot \mathbf{E}(z_{\rm def}, V), \tag{29}$$

and our goal here is to calculate Γ.

We simplify the calculation of the linewidth by describing the fluctuation of charge density indicated in Fig. 4(a) as being the sum of a uniform electron (and hole) density and a fluctuating dipole density—as shown in Fig. 4(b). Therefore, Γ emerges from the standard deviation of a fluctuating dipole density. We calculate $\delta\mathbf{E}$ due to one instance i of a dipole corresponding to the displacement of charges e and $-e$ located at $\mathbf{r}_i \approx (x_i, y_i, z_i)$ and separated by the dipole distances $\mathbf{d}_i$ [see Fig. 4(c)]. Hence, the electric field at $\mathbf{r} = \mathbf{r}_{\rm def}$ produced by the i'th dipole is written as

$$\mathbf{E}_d^i(\mathbf{R}_i) = \frac{e}{4\pi\epsilon R_i^5}\left[3(\mathbf{d}_i\cdot\mathbf{R}_i)\mathbf{R}_i - \mathbf{d}_i R_i^2\right], \tag{30}$$

with $\mathbf{R}_i = \mathbf{r}_i - \mathbf{r}_{\rm def}$ and $R_i = |\mathbf{R}_i|$. The total fluctuating electric field then is given by

$$|\delta\mathbf{E}| = \sqrt{\langle \mathbf{E}_d^2\rangle_t - \langle \mathbf{E}_d\rangle_t^2}, \tag{31}$$

where $\mathbf{E}_d = \sum_{i=1}^{N_{\rm dip}} \mathbf{E}_d^i(\mathbf{R}_i)$ is the total electric field, and $\langle\cdots\rangle_t$ represents the average over the different configurations (realizations), which correspond to the configuration at different times. We assume $\langle \mathbf{E}_d\rangle_t = 0$ due to the large number of dipoles $N_{\rm dip} \gg 1$, the random character of the fluctuations considered, i.e., $\langle \mathbf{d}_i\rangle_t = 0$ and $\langle \mathbf{R}_i\rangle_t = 0$, and the absence of correlation among the random variables we introduce. We evaluate Eq. (31) assuming that the charge displacements $\mathbf{d}_i$ ($d_i = |\mathbf{d}_i|$) are equally and randomly distributed along the x, y, and z axes. Moreover, because of the random character of our variables and $N_{\rm dip} \gg 1$, we choose to rewrite Eq. (31) using a continuous probability distribution for the dipolar position:

$$\delta\mathbf{E}^2 = \int_{\mathcal{V}} d^3r \rho_{\mathcal{V}}(\mathbf{r})\mathbf{E}_d^2(\mathbf{r} - \mathbf{r}_{\rm def}), \tag{32}$$

where $\mathcal{V}$ is the nondepleted volume region within the p-n-n^+ diode and $\rho_{\mathcal{V}}(\mathbf{r})$ is the density of dipoles.

Assuming there is no preferential direction for the total fluctuating electric field $|\delta\mathbf{E}|$, we assume equal fluctuation of the electric field along the x, y, and z axes, with a nominal value along any one axis of $|\delta\mathbf{E}|/\sqrt{3}$. For a linewidth

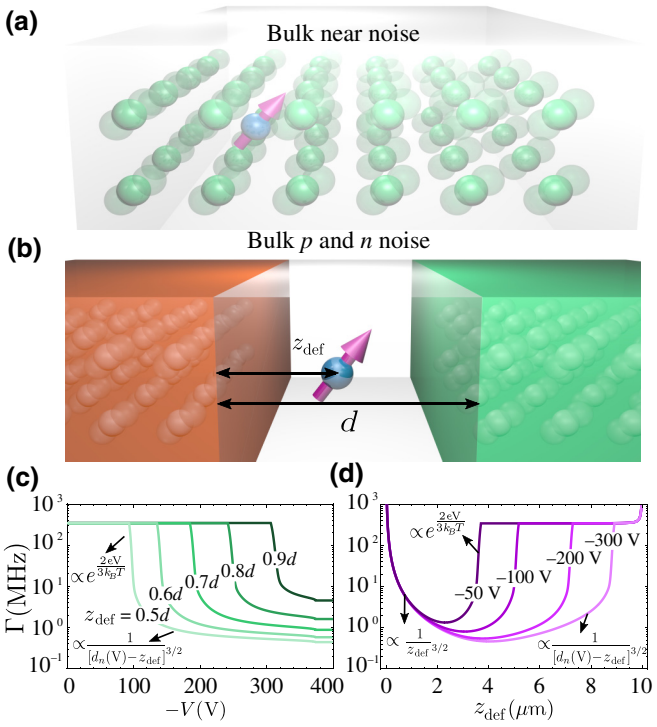

FIG. 5. The electric noise arising from (a) the n region (bulk near noise contribution) and (b) both p and n^+ regions (bulk p and n noise contribution). (c) Broadening Γ as a function of reverse voltage for different $z_{\rm def}$ values due to both the bulk near noise contribution and the bulk p and n noise contribution. (d) Same as (c) as a function of $z_{\rm def}$ for different voltages.

produced mainly due to the fluctuations of the z component of the electric field, we obtain

$$\Gamma = \frac{|\delta\mathbf{E}|}{\sqrt{3}}\left(\mathbf{d}_E^{\rm eff} - \mathbf{d}_G^{\rm eff}\right)\cdot\hat{z}. \tag{33}$$

To obtain the realistic fluctuating electric field $|\delta\mathbf{E}|$ for a device, we assume two different contributions to the electric noise. The first one, which we refer to as "bulk near noise," arises from the fluctuation of the electrons surrounding the defect in the n region [Fig. 5(a)]. The second type, which we refer to as "bulk p and n noise," originates from the fluctuation of electrons and holes within the p and n^+ regions [Fig. 5(b)]. As the spin centers are located far from any surfaces of the diodes, we do not consider sources of noise originating from the surfaces; this will be the topic of future work. In the following subsections we calculate analytically $\delta\mathbf{E}$ [Eq. (32)] arising from the different contributions illustrated in Figs. 5(a) and 5(b).

1. Fluctuating electric field: bulk near noise contribution

In this subsection we estimate the fluctuating electric field $\delta\mathbf{E}_{\mathcal{V}}^{\rm I}$ at $\mathbf{r}_{\rm def} = (x_{\rm def}, y_{\rm def}, z_{\rm def})$ produced by the fluctuation of trapped charges within the nondepleted volume of

the n diode region [Fig. 5(a)]. We evaluate Eq. (32) assuming charge displacements $\mathbf{d}_i$ ($d_i = |\mathbf{d}_i|$) equally distributed along the x, y, and z axes, with density $\rho_{\mathcal{V},\mathrm{I}}(\mathbf{r}) = 1/3\Omega_{\mathcal{V}}^{n}$. For a nondepleted n region we have

$$(\delta\mathbf{E}_{\mathcal{V}}^{\mathrm{I}})^2 = \left(\frac{e}{4\pi\epsilon}\right)^2 \frac{6d_i^2}{3\Omega_{\mathcal{V}}^{n}} \int_0^d dz \int_{-L_x/2}^{L_x/2} dx \int_{-L_y/2}^{L_y/2} dy \frac{1}{R_i^6}. \tag{34}$$

For a diode with dimensions $d, L_x, L_y \gg N^{-1/3}$ and the spin center far from the diode surfaces, we can extend the integral limits to infinity, yielding in spherical coordinates

$$(\delta\mathbf{E}_{\mathcal{V}}^{\mathrm{I}})^2 = 8\pi \left(\frac{e}{4\pi\varepsilon}\right)^2 \frac{d_i^2}{\Omega_{\mathcal{V}}^{n}} \int_{r_c}^{\infty} dr \frac{1}{r^4}, \tag{35}$$

where the cutoff radius, r_c, was introduced to avoid the integral divergence at $r \to 0$. Using $d_i \approx l_{\mathrm{eff}} = \left(\Omega_V^n\right)^{1/3}$, $\Omega_{\mathcal{V}}^{n} = n^{-1}$, and $r_c \approx n^{-1/3}$, we obtain

$$|\delta\mathbf{E}_{\mathcal{V}}^{\mathrm{I}}| \approx \frac{e}{\sqrt{2}\pi\varepsilon} n^{2/3}(z_{\mathrm{def}}, V), \tag{36}$$

where $n(z_{\mathrm{def}}, V)$ is the effective electronic carrier density within region I. This formula, together with Eq. (33), provides essential insight into the general properties of spectral diffusion for emitters. For instance, we are able to predict that the charge density must be below a critical density n_{crit}, i.e.,

$$n < n_{\mathrm{crit}} \approx \left(\frac{\pi\varepsilon\sqrt{6}}{e|\mathbf{d}_E^{\mathrm{eff}} - \mathbf{d}_G^{\mathrm{eff}}|}\Gamma_{\mathrm{lt}}\right)^{3/2}, \tag{37}$$

to suppress the broadening due to spectral diffusion below the broadening due to the emitter's optical transition lifetime, Γ_{lt}. This provides clear guidance for applications of defect emitters, especially in device designs that require a large doping density [48].

Furthermore, there is an upper bound for the electric field, E_{max}, which correspond to the field in the middle of two opposite dipole charges $+e$ and $-e$ separated by approximately l_{eff} [Fig. 4(c)]:

$$\begin{aligned} E_{\mathrm{max}} &= \frac{e}{4\pi\epsilon\,(l_{\mathrm{eff}}/2)^2} + \frac{e}{4\pi\epsilon\,(l_{\mathrm{eff}}/2)^2}, \\ &= \frac{2e}{\pi\epsilon} n^{2/3}(z_{\mathrm{def}}, V). \end{aligned} \tag{38}$$

On the other hand, for an n region partially depleted, we have

$$(\delta\mathbf{E}_{\mathcal{V}}^{\mathrm{I}})^2 = \left(\frac{e}{4\pi\epsilon}\right)^2 \frac{6d_i^2}{3\Omega_{\mathcal{V}}^{n}} \int_{\tilde{d}_n(V) > z_{\mathrm{def}}}^{d} dz \int_{-L_x/2}^{L_x/2} dx \int_{-L_y/2}^{L_y/2} dy \frac{1}{R_i^6}, \tag{39}$$

which for $L_x, L_y \gg N^{-1/3}$ yields

$$(\delta\mathbf{E}_{\mathcal{V}}^{\mathrm{I}})^2 = \left(\frac{e}{4\pi\epsilon}\right)^2 \frac{d_i^2}{3\Omega_{\mathcal{V}}^{n}}\pi \times \left(\frac{1}{\left[\tilde{d}_n(V) - z_{\mathrm{def}}\right]^3} - \frac{1}{\left[\tilde{d}_n(V) - z_{\mathrm{def}} + d\right]^3}\right). \tag{40}$$

Using $d_i \approx l_{\mathrm{eff}} = \left(\Omega_V^n\right)^{1/3}$, $\Omega_{\mathcal{V}}^{n} = N^{-1}$, and $d \gg \tilde{d}_n(V) - z_{\mathrm{def}}$, we obtain

$$\delta\mathbf{E}_{\mathcal{V}}^{\mathrm{I}} \approx \frac{e}{4\pi\epsilon} \frac{\sqrt{\pi}N^{1/6}}{\sqrt{3}} \frac{1}{\left[\tilde{d}_n(V) - z_{\mathrm{def}}\right]^{3/2}}. \tag{41}$$

2. Fluctuating electric field: bulk p and n noise contribution

We now calculate the fluctuating electric field at $\mathbf{r}_{\mathrm{def}}$ due to the fluctuation of trapped charges within n^+ and p regions [Fig. 5(b)]. The procedure is very similar to the one considered in the previous subsection. The only difference regards the limit of the integration of Eq. (34). Here we have to integrate over the nondepleted p and n^+ regions, yielding

$$\begin{aligned} (\delta\mathbf{E}_{\mathcal{V}}^{\mathrm{II}})^2 = &\frac{6d_{i,n^+}^2 \left(\frac{e}{4\pi\epsilon}\right)^2}{3\Omega_{\mathcal{V}}^{n^+}} \int_{d_n(V)}^{d+d_R} dz \int_{-L_x/2}^{L_x/2} dx \int_{-L_y/2}^{L_y/2} dy \frac{1}{R_i^6} \\ &+ \frac{6d_{i,n^p}^2 \left(\frac{e}{4\pi\epsilon}\right)^2}{3\Omega_{\mathcal{V}}^{n^p}} \int_{-d_L}^{-d_p(V)} dz \int_{-L_x/2}^{L_x/2} dx \int_{-L_y/2}^{L_y/2} dy \frac{1}{R_i^6}, \end{aligned} \tag{42}$$

where d_{i,n^+} and d_{i,n^p} are the dipole displacements within the n^+ and p regions, respectively, and $\Omega_{\mathcal{V}}^{n^+}$ and $\Omega_{\mathcal{V}}^{n^p}$ are the densities of dipoles within n^+ and p regions, respectively. Relying on the convergence of the integral, we evaluate it using $L_x, L_y \to \infty$, leading to

$$\begin{aligned} (\delta\mathbf{E}_{\mathcal{V}}^{\mathrm{II}})^2 = &\left(\frac{e}{4\pi\epsilon}\right)^2 \frac{d_{i,n^+}^2}{3\Omega_{\mathcal{V}}^{n^+}}\pi \\ &\times \left(\frac{1}{\left[d_n(V) - z_{\mathrm{def}}\right]^3} - \frac{1}{\left[d_n(V) - z_{\mathrm{def}} + d + d_R\right]^3}\right) \\ &+ \left(\frac{e}{4\pi\epsilon}\right)^2 \frac{d_{i,n^p}^2}{3\Omega_{\mathcal{V}}^{n^p}}\pi \\ &\times \left(\frac{1}{\left[d_p(V) + z_{\mathrm{def}}\right]^3} - \frac{1}{\left[d_p(V) + z_{\mathrm{def}} + d_L\right]^3}\right). \end{aligned} \tag{43}$$

Assuming the defect is closer to the n^+ side with $d_R \gg d$ and using $d_i \approx l_{\text{eff}} = \left(\Omega_{\mathcal{V}}^{n^+}\right)^{1/3}$, with $\Omega_{\mathcal{V}}^{n^+} = N_D^{-1}$, we obtain

$$\delta \mathbf{E}_{\mathcal{V}}^{\text{II}} \approx \frac{e}{4\pi\epsilon} \frac{\sqrt{\pi} N_D^{1/6}}{\sqrt{3}} \frac{1}{[d_n(V) - z_{\text{def}}]^{3/2}}. \tag{44}$$

This expression give us the important quantities to be controlled to produce diodes with reduced broadening of the optical transition energy due to fluctuating electric fields coming from distant regions.

3. Voltage control of the optical emission linewidth

Using the diode densities and dimensions from Fig. 2, we plot in Fig. 5(c) the broadening $\Gamma_{\text{I+II}}$ [Eq. (33)] due to the bulk near noise and bulk p and n noise contributions [Eqs. (40) and (43)] as a function of the voltage. For the bulk near noise contribution, we assume that three quarters of the trapped electrons within the n region are in deep traps, and therefore only one quarter contribute to the fluctuating electric field, i.e., $n(z_{\text{def}}, V) = n_c(z_{\text{def}}, V)/4$. We plot $\Gamma_{\text{I+II}}$ for different spin center positions, from $z_{\text{def}} = 0.5d$ to $z_{\text{def}} = 0.9d$. For a fixed spin center position [Fig. 5(c)], we obtain a constant Γ for voltages $|V| < |V_{\text{th}}|$. This correspond to the situation where the spin center is surrounded by undepleted carrier electrons within the n region, and the optical emission linewidth is mainly due to the bulk near noise contribution [Fig. 5(a)].

As we begin to increase the voltage magnitude $|V| \gtrsim |V_{\text{th}}|$, we deplete the electrons surrounding the spin center. When the depletion region reaches the spin center's position, $n_c \approx e^{eV/k_BT}$ follows from Eq. (14), and we obtain $\Gamma_{\text{I}} \propto e^{2eV/3k_BT}$, which is responsible for the exponential decay of the broadening in Fig. 5(c). For voltages $|V_c| > |V| > |V_{\text{th}}|$, the n region is still not fully depleted, although $n_c(z_{\text{def}}, V) \approx 0$. Hence, we have the broadening due to Eq. (41), $\Gamma_{\text{I}} \propto 1/\left[\tilde{d}_n(V) - z_{\text{def}}\right]^{3/2}$, together with the broadening due to the bulk p and n noise contribution, $\Gamma_{\text{II}} \propto 1/[d_n(V) - z_{\text{def}}]^{3/2}$, following from Eq. (44).

For even larger voltages, $|V| > |V_c|$, the n region becomes completely depleted, and therefore the remaining broadening is due to the bulk p and n noise contribution, $\Gamma_{\text{II}} \propto 1/[d_n(V) - z_{\text{def}}]^{3/2}$. For our diode parameters, $d_n(V) - d \ll d$ [Fig. 2(d)] for $-1000\ \text{V} < V < -100\ \text{V}$, and an approximate independence with regard to the voltage can be seen in Fig. 5(c). In Fig. 5(d) we plot $\Gamma_{\text{I+II}}$ as a function of the spin center's position z_{def} for different reverse voltages, where similar features can be seen.

D. Monte Carlo simulation for the fluctuating electric field

A numerical Monte Carlo simulation yields the fluctuating electric field at the spin center's position for comparison with our analytical results. The results validate the high degree of accuracy of our analytical approach. We numerically simulate the two types of noise contributions illustrated in Fig. 5 using two different approaches. In the first one, a density n (p) of the donors (acceptors) are assumed to have random and uncorrelated fixed positions, with electrons (holes) being randomly placed among the entire region considered in an uncorrelated fashion. In the second approach we specify the electrons' (holes') positions to be constrained within a sphere of radius $n^{-1/3}$ around their corresponding donors' (acceptors') positions, thus capturing the dipole picture illustrated in Fig. 4(b).

1. Bulk near noise contribution

Here we obtain through Monte Carlo simulation the fluctuating electric field due to the bulk near noise contribution [Fig. 5(a)]. We proceed by assuming a spin center placed at the origin $\mathbf{r}_{\text{def}} = (0, 0, 0)$ of a box with dimensions $\mathcal{L} \times \mathcal{L} \times \mathcal{L}$. $\mathcal{N}$ donors are randomly placed within the box (yielding electronic density $n = \mathcal{N}/\mathcal{L}^3$). $\mathcal{N}$ electrons are then randomly placed accordingly to the two different approaches, and finally the total electric field at the spin center's position is calculated. A histogram for the three vector components of the total electric field at the spin center's position is then generated from a series of different electronic distributions in space (realizations). In Fig. 6(a) we present the histogram for the density $n = 4 \times 10^{15}\ \text{cm}^{-3}$, where we use $\mathcal{N} = 1000$ and 2×10^4 different realizations. The best fit to the histogram is obtained for the Student t distribution rather than either the Gaussian distribution or the Lorenztian distribution. Roughly speaking, the Student t distribution differs from the Gaussian (Lorenztian) distribution by its longer tail (broader peak region). This difference is clearly seen in Fig. 6(a), where we have also fitted the data using the three different distributions. The underlying statistical reason for this requires more detailed study, but at this point we suggest this comes from (1) the small number of nearby (influential) electrons (small sampling size) and (2) the electric field assuming large values when electrons are close to the defect, thus increasing the statistical weight of the tail of the distribution. This statistical distribution could be verified and realized experimentally. In our Monte Carlo simulations the positions of electrons for different realizations have no correlation. Therefore, the Student t distribution appears if the fluctuations in the electronic positions have short coherence times.

Figure 6(b) displays the full width at half maximum (FWHM) of the electric field histogram; the bulk noise contribution depends exclusively on the density n. The linewidth Γ (FWHM) resulting from the random electric field distribution is plotted as a function of the density n assuming constrained and unconstrained electronic positions relative to the corresponding donors. For both cases

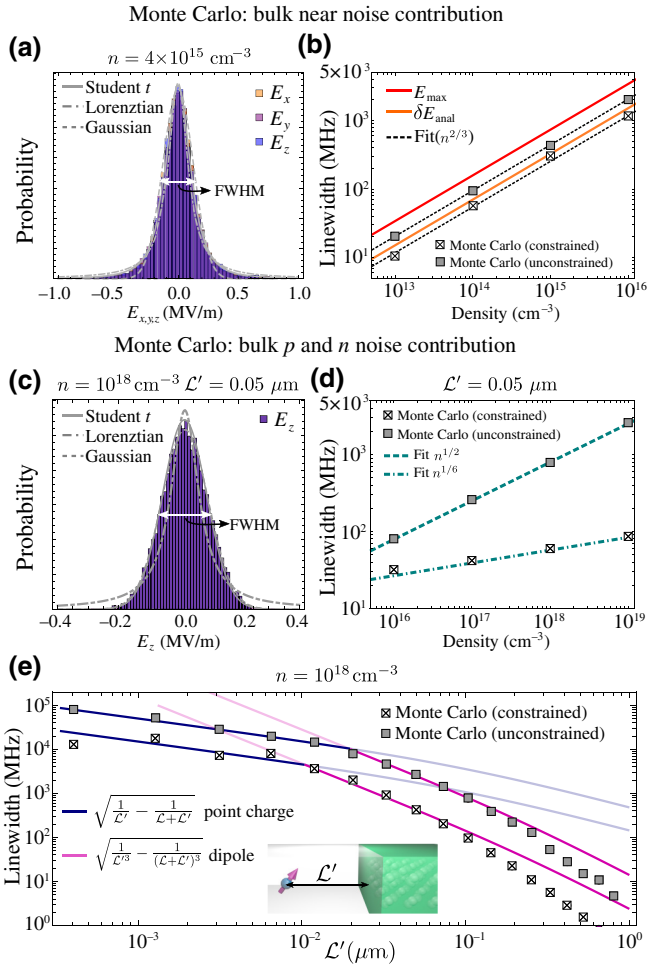

FIG. 6. (a) Electric field histogram due to the bulk near noise contribution with electronic density $n = 4 \times 10^{15}$ cm^{-3}. (b) Bulk near noise FWHM linewidth as a function of density n for constrained and unconstrained electrons' positions. The dashed lines are fits showing their $n^{2/3}$ density dependence, and the orange (red) line is the plot of the analytical result given by Eq. (36) [Eq. (38)] (c) Electric field histogram due to the bulk n noise contribution for electronic density $n = 10^{18}$ cm^{-3} and $\mathcal{L}' = 0.05$ μm. (d) Bulk n noise FWHM linewidth as a function of density n for constrained and unconstrained electrons' positions for $\mathcal{L}' = 0.05$ μm. (e) Bulk near n noise FWHM linewidth as a function of $\mathcal{L}'$ for $n = 10^{18}$ cm^{-3}.

the fit to the numerical data shows an $n^{2/3}$ dependence on the linewidth, which is explained by the analytical derivation presented in the previous section [Eq. (36)]; in this regime this also agrees with the Monte Carlo simulation reported in Ref. [81]. We thus find that the density dependence of the bulk near noise is unlikely to be dependent on the details of the fluctuation character. In addition, we also plot the linewidth [Eq. (33)] arising from Eqs. (36) and (38), where we see good agreement between the analytical theory and the Monte Carlo simulation.

2. Bulk n and p noise contribution

Here we study the fluctuating electric field due to the bulk p and n noise contribution [Fig. 5(b)]. We use the same procedure as in the previous section, with the only difference having now a spin center located outside the box, i.e., $\mathbf{r}_{\rm def} = (0, 0, \mathcal{L}' + \mathcal{L}/2)$. In Fig. 6(c) we plot the histogram for the z component of the electric field, E_z, for $n = 10^{18}$ cm^{-3} ($\mathcal{N} = 1000$ and $\mathcal{L} = 0.1$ μm) and $\mathcal{L}' = 0.05$ μm. A long distribution tail is no longer visible, which is consistent with having the spin center far from the electrons, thus imposing an upper bound to the maximum electric field at $\mathbf{r}_{\rm def}$. The Lorenztian remains a poor fit for our electric field histogram; however, the differences between the Student t distribution and the Gaussian distribution become less noticeable. However, a close look at the maximum of the histogram reveals that the Student t distribution still produces a better fit.

In Fig. 6(d) we plot the linewidth of the electric field distribution as a function of the density, assuming constrained and unconstrained electronic positions, for $2\mathcal{L}' = \mathcal{L} = 0.1$ μm. Unlike our expectations from bulk near noise, here the constrained and unconstrained situations yield a different linewidth dependence on the density n; the constrained case yields the dependence $n^{1/6}$, whereas the unconstrained case yields a larger linewidth with $n^{1/2}$ dependence. We emphasize that for constrained electrons, a case that captures the dipole character of the process described in Fig. 4(b), we obtain the same density dependence as the analytical formula [Eq. (44)]. On the other hand, the $n^{1/2}$ dependence for the unconstrained case can be easily derived if instead of using Eq. (32) for a continuous probability of dipoles, we use it for a continuous probability of point electron and hole densities $\rho_p(\mathbf{r})$, with electric field $\mathbf{E}_p(\mathbf{R}) = \pm(e/4\pi\epsilon)(\mathbf{R}/|\mathbf{R}|^3)$, i.e.,

$$\delta\mathbf{E}_p^2 = 2\int_{\mathcal{V}} d^3r \rho_p(\mathbf{r})\mathbf{E}_p^2(\mathbf{r} - \mathbf{r}_{\rm def}). \tag{45}$$

Assuming again the x and y integration limits are taken to infinity, we obtain for the bulk n noise contribution

$$|\delta\mathbf{E}_p| = \frac{e}{\sqrt{2\pi\epsilon}} n^{1/2} \sqrt{\frac{1}{\mathcal{L}'} - \frac{1}{\mathcal{L} + \mathcal{L}'}}, \tag{46}$$

which agrees with the Monte Carlo results in Fig. 6(d). Finally, the smaller linewidth produced by the constrained situation is traced to the smaller electric fields from the dipole field compared with those of point charges.

In Fig. 6(e) we plot the linewidth dependence on $\mathcal{L}'$ for both constrained and unconstrained electrons' positions with $n = 10^{18}$ cm^{-3}. For the case of constrained electrons, the linewidth shows a $\sqrt{1/\mathcal{L}'^3 - 1/(\mathcal{L} + \mathcal{L}')^3}$ dependence for $\mathcal{L}' > 0.1$ μm, which agrees with our analytical derivation for dipoles, Eq. (43). On the other hand, for $\mathcal{L}' < 0.1$ μm, the numerical data show a dependence

on $\sqrt{1/\mathcal{L}' - 1/(\mathcal{L}+\mathcal{L}')}$ instead, which is a scaling characteristic of the point charge distribution as shown by Eq. (46). Although this may appear to contradict the constrained character of the simulation, the dipole character manifests itself only at distances $\mathcal{L}'$ much larger than the dipole distance $n^{-1/3} \approx 0.01$ μm, and therefore a dependence according to the expression for point charges is expected for small values of $\mathcal{L}'$. Unconstrained electrons show the same scaling behavior as the constrained ones, with the only difference being a different overall constant factor. Since there is no constraint between electrons and donors, for small values of $\mathcal{L}'$ we do obtain the scaling $\sqrt{1/\mathcal{L}' - 1/(\mathcal{L}+\mathcal{L}')}$ of point charges, which agrees with our theory [Eq. (46)]. However, for larger $\mathcal{L}'$ distances, the linewidth also scales with the dipole $\sqrt{1/\mathcal{L}'^3 - 1/(\mathcal{L}+\mathcal{L}')^3}$ form [Eq. (43)] even though no constraint on electron position was imposed. Thus, the dipole assumption used in the previous analytical section provides a good picture for the effects of charge noise on the linewidth. Finally, for spin centers farther away than the box dimension $\mathcal{L}$, i.e., $\mathcal{L}' > 0.1$ μm, the infinity limits taken on the x and y integration are not valid anymore, and a deviation from the analytical curve is seen.

E. Photoluminescence frequency and linewidth

The full dependence of the linewidth with respect to the temperature, electronic and hole densities, voltages, and position of the defect is obtained through Eq. (33), with the fluctuating electric fields calculated through Eqs. (40) and (43). Therefore, using the frequency shift expressions [Eqs. (24)–(26)] together with the predicted linewidth [Eq. (33)] we have a full theoretical characterization of the photoluminescence, including the linewidth, from a divacancy represented by Eq. (28). In Fig. 7(a), we plot the calculated PL as a function of the voltage for the (kk) defect in Fig. 3(a). In our theoretical plot we consider both $|E_y\rangle \to |T_0\rangle$ and $|E_{1,2}\rangle \to |T_\pm\rangle$ (kk) transitions. The corresponding experimental PL data for these transitions [1] are shown in Fig. 7(b). Here, we have the (kk) defect located at $z = 4.42$ μm (corresponding to $V_{\rm th} \approx -70$ V and $N = 4 \times 10^{15}$ cm^{-3}), with $d_E^{\parallel} - d_G^{\parallel} = 3.25$ GHz/MV m and $E_{E_y} - E_G = -0.8$ GHz for the $|E_y\rangle \to |T_0\rangle$ transition, and $d_E^{\parallel} - d_G^{\parallel} = 3.55$ GHz/MV m with $E_{E_1} - E_G = 0.6$ GHz and $E_{E_2} - E_G = 0.1$ GHz for the $|E_{1,2}\rangle \to |T_\pm\rangle$ transitions. We emphasize that these dipole values differ from the ones fitted in Fig. 3 due to the smaller fitting voltage range of Fig. 7. As before we assume that only one quarter of the carriers contribute to the fluctuating electric field due to deeper trapping effects, i.e., $n_{\rm eff}(z_{\rm def}, V) = n_c(z_{\rm def}, V)/4$. We emphasize, however, that different ratios also reproduce well the experimental data (see Appendix B and Fig. 10). For voltages $|V| < |V_{\rm th}|$ the spin center is outside the depletion region, and thus experiencing zero electric field and hence a zero frequency shift, in addition to large electric noise, which leads to a large linewidth $\Gamma \approx 0.5$ GHz. For $|V| > |V_{\rm th}|$ the carriers surrounding the spin center start to become depleted, allowing the spin center to experience a nonzero electric field and smaller fluctuating electric noise from the fewer carriers, leading to a shifted optical emission frequency and a narrower linewidth. Because of the large diode dimensions $L_x, L_y \approx 100$ μm in Ref. [1], noise from the surfaces does not play any role and it is ignored in Fig. 7. A very smooth linewidth transition around $V_{\rm th}$ is found in the experimental data. Good agreement between theory and experiment is found by assuming an electronic temperature around the defect of approximately 300 K, produced by the laser illumination. The higher the temperature, the longer the tail of electronic density around the defect $[n_c(z_{\rm def}, V \approx V_{\rm th}) \propto e^{-eV/k_BT}]$, which is the underlying reason for the smooth linewidth transition as $\Gamma_I \propto n_c^{2/3} \approx e^{-(2/3)(eV/k_BT)}$; see Fig. 4(g).

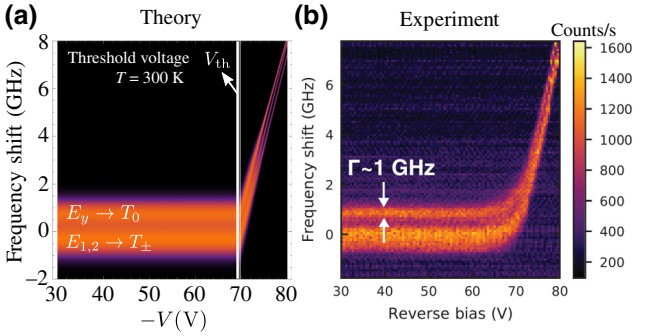

FIG. 7. Comparison between theory (a) and experimental data from Ref. [1] (b) [reprinted with permission from AAAS] for photoluminescence of a single (kk) divacancy with $|E_y\rangle \to |T_0\rangle$ and $|E_{1,2}\rangle \to |T_\pm\rangle$ addressed transitions. For $|V| < |V_{\rm th}|$ the (kk) defect is within the nondepleted part of the n region, thus experiencing zero electric field and large electric noise and linewidth. For $|V| > |V_{\rm th}|$ the charges begin to be depleted around the spin center, yielding a narrowing of the linewidth, and a shift in frequency in response to the now present electric field.

V. SPIN DECOHERENCE DUE TO ELECTRIC NOISE

Spin decoherence processes produce a continuous loss of the memory of an initial state due to the influence of and interaction with an environment. In this section we study the decoherence of a single defect spin within a diode device. For our case, the fluctuating electric field produces—in addition to the emission spectrum linewidth we have evaluated already—spin decoherence [see Fig. 8(a)]. The random fluctuating electric fields produce a set of random phases in the wave function of the spin state. After averaging these random phases, we obtain a corresponding exponential temporal decay of the state amplitude.

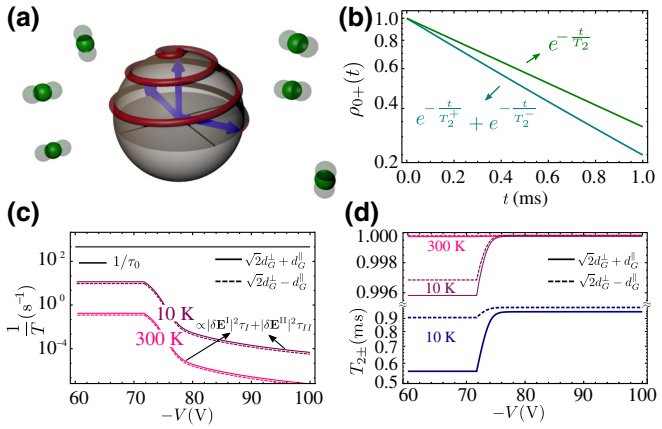

FIG. 8. (a) Spin dephasing leading to decoherence due to the fluctuating electric charges. (b) Comparison between single-exponential and biexponential decoherence processes. (c) Decoherence contributions in Eq. (66) as a function of diode voltage. (d) Increase of $T_{2\pm}$ decoherence time as a function of voltage due to the reduction of the electric noise. The dark blue curve is plotted exaggerating the $d_G^\parallel$ and $d_G^\perp$ (τ^1) dipole values by a factor of approximately 10 (100). In (c),(d) the solid (dashed) lines represent the contributions within $T_{2\pm}$ proportional to $\sqrt{2}d_G^\perp + d_G^\parallel$ ($\sqrt{2}d_G^\perp - d_G^\parallel$).

We find that for defects with C_{3v} point group symmetry, the precise spin decoherence process can be addressed correctly only through a 3×3 spin-1 formalism, which includes the whole GS manifold. This in turn leads to a *biexponential* decoherence process that cannot be obtained through the usual 2×2 spin-1/2 formalism [5,7–9,11,17]. The complexity of the spin-1 manifold has been discussed phenomenologically before (e.g., Ref. [13]); however, here we describe how the structure and temporal behavior of this decoherence emerge from microscopic models of electric noise. Finally, we obtain analytical formulas for the spin coherence times as a function of the temperature, defect position, diode voltages, diode dimensions, and diode densities. These provide a good understanding of how the electric noise competes with other noise types, and also provide the nominal densities below which the decoherence due to the electric noise is suppressed.

A. Spin-1 formalism for the decoherence of defects with C_{3v} point group symmetry

Here we apply the already-evaluated time-dependent fluctuating field due to the fluctuations of charges illustrated in Figs. 4 and 5, yielding $\mathbf{E}(z,t) = \mathbf{E}(z) + \delta\mathbf{E}(t)$, with average in time $\langle \delta\mathbf{E}(t) \rangle_t = 0$ and deviation $|\delta\mathbf{E}| = \sqrt{\langle \delta\mathbf{E}(t)^2 \rangle_t}$ [Eq. (31)]. Therefore, the GS Hamiltonian of a defect with C_{3v} symmetry can be written as the sum of time-dependent and time-independent terms:

$$\mathcal{H}_{\rm GS}^{3v}(t) = \mathcal{H}_{\rm GS}^{3v} + \mathcal{H}'(t), \tag{47}$$

where $\mathcal{H}_{\rm GS}^{3v}$ is given by Eq. (1) and

$$\frac{\mathcal{H}'(t)}{h} = d_G^\perp \delta E_x(t) \left(S_y^2 - S_x^2\right) + d_G^\perp \delta E_y(t) \left(S_x S_y + S_y S_x\right) + d_G^\parallel \delta E_z(t) \left(S_z^2 - \frac{2}{3}\right). \tag{48}$$

For NV centers and (hh) and (kk) divancancies oriented along the diode direction (z axis), the only relevant component of the dc electric field is along the z axis. For this case, the eigenstates of $\mathcal{H}_{\rm GS}$ are still given by $|T_-\rangle$, $|T_0\rangle$, and $|T_+\rangle$. We emphasize that the analyses and results presented here are valid only for small magnetic fields since a degeneracy of the triplet states $|T_\pm\rangle$ was assumed. We now consider a general initial coherent state $|\psi\rangle\,(t=0) = |\psi\rangle_0 = a_-|T_-\rangle + a_0|T_0\rangle + a_+|T_+\rangle$, and let it evolve in time in the presence of the total Hamiltonian [Eq. (47)]. After time t, the initial state $|\psi\rangle_0$ is given by the Magnus expansion in leading order

$$\begin{aligned} |\psi\rangle\,(t) &= e^{\sum_{k=1}^{2} \Omega_k(t)} |\psi\rangle_0\,, \\ &= a_-(t)|T_-\rangle + a_0(t)|T_0\rangle + a_+(t)|T_+\rangle\,, \end{aligned} \tag{49}$$

with

$$\Omega_{k=1}(t) = \frac{1}{i\hbar}\int_0^t dt' \mathcal{H}_{\rm GS}^{3v}(t') \tag{50}$$

$$\Omega_{k=2}(t) = \frac{1}{2(i\hbar)^2}\int_0^t \int_0^{t'} dt'dt'' \left[\mathcal{H}_{\rm GS}^{3v}(t'), \mathcal{H}_{\rm GS}^{3v}(t'')\right] \tag{51}$$

and the corresponding density matrix $\hat{\rho}(t) = \sum_{\mu,\nu=-,0,+} a_\mu^*(t)\, a_\nu(t)\, |T_\nu\rangle\langle T_\mu|$, which represents the system that has evolved for a time t from the initial state. We now average over the ensemble of fluctuating electric charge configurations illustrated in Fig. 5, yielding

$$\langle\hat{\rho}(t)\rangle = \begin{pmatrix} \rho_{--}(t) & \rho_{-0}(t) & \rho_{-+}(t) \\ \rho_{0-}(t) & \rho_{00}(t) & \rho_{0+}(t) \\ \rho_{+-}(t) & \rho_{+0}(t) & \rho_{++}(t) \end{pmatrix}, \tag{52}$$

with $\rho_{\nu\mu}(t) = \langle a_\mu^*(t)\, a_\nu(t)\rangle$. In this work we present the analytical result for the most general initial coherent state $|\psi\rangle_0 = a_-|T_-\rangle + a_0|T_0\rangle + a_+|T_+\rangle$, with $|a_-|^2 + |a_0|^2 + |a_+|^2 = 1$ arising from the normalization. For this particular case, the $a_\nu(t)$ coefficients are given by

$$\frac{a_-(t)}{e^{-i(E_-/\hbar)t}} = \frac{1}{2}F\left(-\frac{d_\parallel}{3},t\right)\left\{a_-\left[F\left(\sqrt{2}d_\perp,t\right)+F\left(-\sqrt{2}d_\perp,t\right)\right]-a_+e^{i(\pi/4)}\left[F\left(\sqrt{2}d_\perp,t\right)-F\left(-\sqrt{2}d_\perp,t\right)\right]\right\}, \quad (53)$$

$$\frac{a_0(t)}{e^{-i(E_0/\hbar)t}} = a_0F\left(\frac{2d_\parallel}{3},t\right), \quad (54)$$

$$\frac{a_+(t)}{e^{-i(E_+/\hbar)t}} = \frac{1}{2}F\left(-\frac{d_\parallel}{3},t\right)\left\{a_+\left[F\left(\sqrt{2}d_\perp,t\right)+F\left(-\sqrt{2}d_\perp,t\right)\right]-a_-e^{i(\pi/4)}\left[F\left(\sqrt{2}d_\perp,t\right)-F\left(-\sqrt{2}d_\perp,t\right)\right]\right\}, \quad (55)$$

where we have defined $F(\gamma,t)\equiv e^{i\gamma\int_0^t dt'\delta E(t')}$. To obtain these expressions we assume the fluctuating fields along the x, y, and z axes, $\delta E_x(t)$, $\delta E_y(t)$, and $\delta E_z(t)$, all have the same statistical properties (e.g., mean, deviation, and correlation function), and hence $\delta E_x(t),\delta E_y(t),\delta E_z(t)\equiv\delta E(t)$. To calculate the matrix elements of Eq. (52), we average the product $\langle F(\gamma,t)F(\delta,t)\rangle = \left\langle e^{i(\gamma+\delta)\int_0^t dt'\delta E(t')}\right\rangle = \langle F(\gamma+\delta,t)\rangle$. This average is obtained by rewriting the exponential as an infinite series, and computing the average of its individual components. Assuming that $\delta E(t)$ follows a Gaussian probability distribution, we obtain

$$\left\langle e^{i\gamma\int_0^t dt'\delta E(t')}\right\rangle = e^{-(\gamma^2/2)\int_0^t\int_0^t dtdt''\langle\delta E(t')\delta E(t'')\rangle}. \quad (56)$$

To compute Eq. (56) we require the correlation function of the total fluctuating electric field at different times, $S(\tau,\tau')=\langle\delta E(\tau)\delta E(\tau')\rangle$, and assume temporal transitional symmetry $S(\tau'-\tau)=S(\tau,\tau')$. It is also sufficient to know the noise spectral density $S(\omega)$, which is related to $S(t)$ through the Fourier transform $S(\tau'-\tau)=\int_{-\infty}^{\infty}(d\omega/2\pi)S(\omega)e^{i\omega(\tau'-\tau)}$. Here we assume the total spectral density is described by the sum of two different Lorenztian noise spectral densities, arising from the two different sources of fluctuating electric charges, such as those illustrated in Figs. 5(a) and 5(b). Thus,

$$S(\omega)=\sum_\eta\frac{2(\delta\mathbf{E}^\eta)^2}{3}\frac{\tau_\eta}{1+\omega^2\tau_\eta^2}, \quad (57)$$

where the index η stands for the different noise contributions, τ_η represents the corresponding correlation time, and $\delta\mathbf{E}^\eta$ represents the corresponding fluctuating electric field, given by Eqs. (40) and (43). The correlation function thus reads $S(t)=\frac{1}{3}\sum_\eta(\delta\mathbf{E}^\eta)^2e^{-|t|/\tau_\eta}$ and for $t\gg\tau_\eta$ yields [82]

$$\left\langle e^{i\gamma\int_0^t dt'\delta E(t')}\right\rangle \approx e^{-t(\gamma^2/3)\sum_\eta(\delta\mathbf{E}_\eta)^2\tau_\eta}. \quad (58)$$

Finally, using Eq. (58), we obtain the diagonal terms

$$\rho_{00}(t)=a_0^2, \quad (59)$$

$$\rho_{--}(t)=\frac{1}{2}\left[|a_-|^2+|a_+|^2+\left(|a_-|^2-|a_+|^2\right)e^{-t/T_1}\right], \quad (60)$$

$$\rho_{++}(t)=\frac{1}{2}\left[|a_-|^2+|a_+|^2-\left(|a_-|^2-|a_+|^2\right)e^{-t/T_1}\right], \quad (61)$$

with characteristic longitudinal decay time

$$\frac{1}{T_1}=\left(2\sqrt{2}\tilde{d}_G^\perp\right)^2\frac{1}{3}\sum_\eta(\delta\mathbf{E}^\eta)^2\tau_\eta+\frac{1}{\tau_0}, \quad (62)$$

with $\tilde{d}_G^\perp=d_G^\perp/2\pi$, and the off-diagonal terms

$$\rho_{0-}(t)=\frac{a_0e^{i\omega_{-0}t}}{2}\left[\left(a_-^*+e^{-i\pi/4}a_+^*\right)e^{-t/T_{2+}}+\left(a_-^*-e^{-i\pi/4}a_+^*\right)e^{-t/T_{2-}}\right], \quad (63)$$

$$\rho_{0+}(t)=\frac{a_0e^{i\omega_{+0}t}}{2}\left[\left(a_+^*+a_-^*e^{-i\pi/4}\right)e^{-t/T_{2+}}+\left(a_+^*-a_-^*e^{-i\pi/4}\right)e^{-t/T_{2-}}\right], \quad (64)$$

$$\rho_{-+}(t)=\frac{1}{2}\left[a_-^*a_++a_-a_+^*+\left(a_-a_+^*-a_-^*a_+\right)e^{-t/T_{2a}}\right], \quad (65)$$

with $\omega_{\mu\nu}=E_\mu-E_\nu$, and the following transverse decay times:

$$\frac{1}{T_{2\pm}}=\left(\sqrt{2}\tilde{d}_G^\perp\pm\tilde{d}_G^\parallel\right)^2\frac{1}{3}\sum_\eta(\delta\mathbf{E}^\eta)^2\tau_\eta+\frac{1}{\tau_0}, \quad (66)$$

with $\tilde{d}_G^{\parallel} = d_G^{\parallel}/2\pi$, and

$$\frac{1}{T_{2a}} = \left(2\sqrt{2}\tilde{d}_G^{\perp}\right)^2 \frac{1}{3}\sum_{\eta}(\delta\mathbf{E}^{\eta})^2\,\tau_{\eta} + \frac{1}{\tau_0}. \tag{67}$$

We emphasize that in Eqs. (60)–(65), the intrinsic decoherence time τ_0 was introduced to incorporate other spin decoherence mechanisms that were not taken into account in our approach, e.g., dephasing from the random hyperfine nuclear fields of the surrounding atoms [43]. This is an important element to add since in the absence of τ_0 our approach would permit an infinite decoherence time as $|\delta\mathbf{E}^{\eta}| \to 0$. It is also important to emphasize that differently from many studies [5,7–9,11,17], here we do not find only one transverse decay characteristic time, but rather find four different ones, given by Eqs. (66) and (67).

A further analysis of Eqs. (63)–(65) shows that $\rho_{-+}(t)$ has a decay time approximately 4 times faster than $\rho_{0-}(t)$ and $\rho_{0+}(t)$ ($T_{2a} \ll T_{2\pm}$), and therefore we assume $\rho_{-+}(t) \approx 0$. For the particular case of special experimental relevance, $a_- = 0$ ($a_+ = 0$), we see that $\rho_{0-}(t)$ [$\rho_{0+}(t)$] [Eq. (63)] is given by the difference of two exponentials with similar arguments, so we also assume $\rho_{0-}(t) \approx 0$ [$\rho_{0+}(t) \approx 0$]. With those two approximations, $\rho_{0+}(t)$ [$\rho_{0-}(t)$] is the term responsible for the decoherence. Surprisingly this term contains *biexponential relaxation*—rather than a single exponential—with characteristic times given by Eq. (66).

In Fig. 8(b) we plot $\rho_{0+}(t)$ with $T_{2+} \neq T_{2-}$ and $T_{2+} = T_{2-} = T_2$. We observe that the biexponential deviates from the linear trend within the log plot, which could be easily seen in experiments. The biexponential also produces a faster decay compared with the case with $T_{2+} = T_{2-} = T_2$. The unusual biexponential feature appears due to the presence of the $d_G^{\perp}$ dipole term. Setting $d_G^{\perp} = 0$, leading to $T_{2+} = T_{2-}$, produces the same single-exponential decay as the 2×2 formalism.

The biexponential relaxation feature emerges as the sum of two different decoherence processes. The first happens due to the dephasing of the initial state through the diagonal Hamiltonian terms that are proportional to $d_G^{\parallel}\delta E(t)$ [see Eq. (48)], while the second happens due to the off-diagonal $d_G^{\perp}\delta E(t)$ terms, which couple the $|T_+\rangle$ and $|T_-\rangle$ subspaces. The presence of these off-diagonal terms allows an additional dephasing process, in which the loss of the memory of the initial state happens between the coupled $|T_+\rangle$ and $|T_-\rangle$ subspaces. As a consequence of this coupling we observe an increase of the population of the $|T_-\rangle$ state, $\rho_{--}(t)$ [Eq. (60)], which increases in time solely due to the presence of $d_G^{\perp} \neq 0$ within T_1. The 3×3 density matrix formalism for the spin-1 system is necessary to obtain this biexponential relaxation process. If we had excluded the $|T_-\rangle$ state due to its absence in the initial state $|\psi\rangle_0$, we would not obtain the two longitudinal dephasing times nor the increase of the $|T_-\rangle$ population. Most importantly, for NV centers and 4H-SiC divacancies we have $d_G^{\perp} \gg d_G^{\parallel}$ [42], and thus the decoherence time is dominated by the $d_G^{\perp}$ term, which is not present in the 2×2 formalism. Moreover, the results of the 2×2 spin-1/2 formalism can be easily recovered from our formalism when $d_G^{\perp} = 0$, which leads to $T_{2+} = T_{2-}$, $T_{2a} = 0$, and $\rho_{0-}(t) = \rho_{-+}(t) = \rho_{--}(t) = 0$.

B. Decoherence times as a function of diode voltage

To evaluate how the decoherence times obtained in the previous subsection respond to the diode voltage via Eq. (66), the correlation times of the fluctuating electric fields, τ_{η}, are required. There are two different correlation times, which are associated with the bulk near noise and the bulk p and n^+ noise contributions, shown in Figs. 5(a) and 5(b), respectively. To estimate those quantities, we assume $T = 10$ K for the electron temperature within the p and n^+ regions (experimental lattice temperature in Ref. [1]) and either $T = 10$ K or $T = 300$ K for the electrons within the n region, due to the laser illumination. The estimate for τ_{η} comes from the relation between the mobility μ and the diffusion coefficient $\mathcal{D}$ for electrons and holes. For 4H-SiC, $\mu_{10\,\mathrm{K}} \approx 15$ cm^2/V s and $\mu_{300\,\mathrm{K}} \approx 70$ cm^2/V s [83]. Using the relation $\mathcal{D} = (\mu/e)k_BT$ and assuming $\mathcal{D} \approx l_{\mathrm{eff}}^2(1/\tau_{\eta})$, with the distance between trapped centers given by $l_{\mathrm{eff}} \approx n_{\mathrm{eff}}^{-1/3}$, we can establish a relation between the effective charge densities n_{eff} and the correlation time, namely, $\tau_{\eta} = (e/\mu k_BT)n_{\mathrm{eff}}^{-2/3}$. Finally, we obtain $\tau_{\mathrm{I}}^{10\,\mathrm{K}} \approx 8$ ns and $\tau_{\mathrm{I}}^{300\,\mathrm{K}} \approx 55$ ps for $n_{\mathrm{eff}} = 1 \times 10^{15}$ cm^{-3}, and $\tau_{\mathrm{II}}^{10K} \approx 16$ ps for p and n^+ densities of approximately 10×10^{18} cm^{-3}.

In Fig. 8(c) we plot the different contributions of $1/T_{2\pm}$ [Eq. (66)] as a function of the diode voltage V for the characteristic times estimated above. The solid (dashed) lines correspond to the term proportional to $\sqrt{2}d_G^{\perp} + d_G^{\parallel}$ ($\sqrt{2}d_G^{\perp} - d_G^{\parallel}$) within $1/T_{2+}$ ($1/T_{2-}$). Here we use the same diode parameters as in Fig. 7(a), where the spin center is located at $z = 4.42$ μm, with corresponding $V_{\mathrm{th}} \approx -70$ V. We assume $\tau_0 = 1$ ms, consistent with recent reported values [43]. Because of the dipole inequality $d_G^{\perp} \gg d_G^{\parallel}$ following from $d_G^{\perp} \approx 30 \times 10^{-2}$ Hz/V m and $d_G^{\parallel} \approx 3 \times 10^{-2}$ Hz/V m [84], we barely see a difference regarding the different contributions proportional to $\sqrt{2}d_G^{\perp} \pm d_G^{\parallel}$, thus yielding $T_{2+} \approx T_{2-}$ (and no evident biexponential relaxation). For $|V| < |V_{\mathrm{th}}|$, the spin center is placed outside the depletion region, thus experiencing large electric bulk near noise that yields a large $(d_G^{\perp}\delta\mathbf{E}^{\mathrm{I}})^2\tau_I$ contribution. On the other hand, for $|V| > |V_{\mathrm{th}}|$ the depletion region reaches the spin center, and we start seeing a suppression of the bulk near noise and a consequent decrease of $(d_G^{\perp}\delta\mathbf{E}^{\mathrm{I}})^2\tau_I$,

similar to the narrowing of the PL linewidth in Fig. 7. However, because of the short characteristic times $\tau_\eta \lesssim 10$ ns, we see that the bulk noise contributions are 3–5 orders of magnitude smaller than ${\tau_0}^{-1}$, thus showing the electric noise is irrelevant for decoherence for these parameters. This can also be seen in Fig. 8(d), where we plot $T_{2\pm}$ as a function of the voltage for 10 and 300 K for the n region (purple and pink curves, respectively). The increase of the coherence time due to the reduction of the surrounding electric noise is very small. Therefore, for the diode setup in Ref. [1], we should not observe an increase of the coherence time after depletion of the bulk near fluctuations. This result agrees with the measurements reported in Ref. [1], which did not observe any increase of T_2 for $|V| > |V_{\rm th}|$. An important implication of this finding is the potential to use divacancies embedded in gated diode devices as a possible way to realize qubits without having the drawback of susceptibility to the electric noise arising from the charged diode regions. Similarly, we can also extrapolate this application to qubit divacancies under nearby electrical gates. Furthermore, we see that the T_2 decoherence process due to the electric bulk near noise will be suppressed only for fluctuating electric fields and correlation times satisfying

$$|\delta \mathbf{E}_{\rm I}|^2 \tau_{\rm I} < \frac{1/\tau_0}{\frac{1}{3}\left(\sqrt{2}d_G^{\perp} \pm d_G^{\parallel}\right)^2} \tag{68}$$

which with the use of Eq. (36) can be expressed as

$$n^{4/3}\tau_{\rm I} < \frac{1/\tau_0}{(e^2/6\pi^2\varepsilon^2)\left(\sqrt{2}d_G^{\perp} \pm d_G^{\parallel}\right)^2}, \tag{69}$$

which establishes a relation among the suppression of the electric noise in terms of electronic density, correlation time, and defect electric dipole moment. Using this formula, we note that if the electric dipole constant is approximately 10 times larger, or if the correlation time is approximately 100 longer, we would observe a clear increase of the coherence time after depletion of the region surrounding the spin center. This is shown by the dark blue curve in Fig. 8(d), where we assume $d_G^{\perp} \approx 300 \times 10^{-2}$ Hz/V m and $d_G^{\parallel} \approx 200 \times 10^{-2}$ Hz/V m. In addition, with the new values for the dipole constants, we also see a clear difference between T_{2-} and T_{2+}, which in turn would lead to an evident biexponential relaxation process.

VI. CONCLUSIONS

We provide a thorough and complete analytical and numerical theoretical description of the optical and electronic properties of a spin center in the presence of a dc electric field and local charge depletion produced through a voltage applied across a p-n-n^+ diode. Our results are in good agreement with the experimental measurements reported in Ref. [1], and provide a more detailed understanding of the structure and properties of the materials used in the diode. The diode structure allows precise control of the spin center's optical emission (PL) frequencies. Analytical expressions for the spin center's transition frequencies are obtained as a function of the applied voltage and the diode parameters, which allows us to extract not only the electric dipole constants but also the spin center's position within the diode. We propose practical 4H-SiC diode parameters that would allow frequency shifts of the PL in the terahertz range without dielectric breakdown. Moreover, the creation of the depletion region around the spin center's position removes electric noise from charges near the spin center, thus narrowing the spin center's PL linewidth, which we calculate analytically and simulate numerically, with similar results. Finally, we introduce a spin-1 formalism for the decoherence process of a spin center's ground state that yields a biexponential spin decoherence from microscopic models of electric field noise, and explain why this has not yet been seen experimentally for spin centers in diodes; however, for closely related systems it should be possible to both observe these features and increase the spin coherence time through local charge depletion. We show that for typical diode designs and densities, the electric noise arising from the p, n, and n^+ regions does not substantially shorten the spin defect coherence times, thus creating a possible path for qubit manipulation with gated diode structures. In addition, the possibility of large tunable Stark shifts (on the order of terahertz) accompanied by a corresponding small linewidth (approximately 20 MHz) and small decoherence rate makes this system an excellent candidate for a single-photon source. For instance, for SiC divacancy frequency shifts of approximately 2 THz with corresponding linewidths of approximately 20 MHz, it is possible to obtain shift-to-linewidth ratios of approximately 10^5, the highest within solid-state single-photon-emission sources [1]. Finally, none of the theoretical results presented in this paper disagree with recent experimental results [1].

ACKNOWLEDGMENTS

We thank D.D. Awschalom, C.P. Anderson, A. Bourassa, P.E. Faria, G.D. Fuchs, S.R. McMillan, A.R. da Cruz, T. de Campos, Kwangyul Hu, C. Şahin, and B.S.C. Candido for useful discussions. This work was supported by the U.S. Department of Energy, Office of Basic Energy Sciences, under Award No. DE-SC0019250.

The authors disclose their intention to commercialize the software used for the calculations presented in this work.

APPENDIX A: FREQUENCY SHIFT FOR ALTERNATIVE DENSITIES

For completeness, in Fig. 9 we also show the fit of the (kk), (hh), and (kh) divacancy frequency shifts in Fig. 3

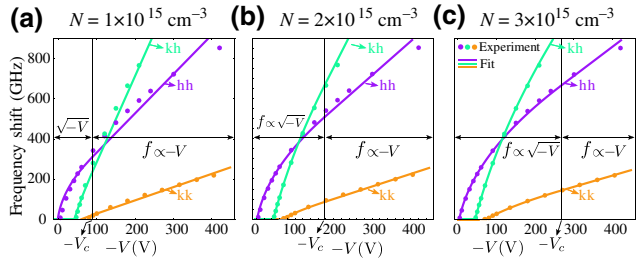

FIG. 9. Fit for the frequency shift versus voltage V for the $|E_y\rangle \rightarrow |T_0\rangle$ and $|E_{1,2}\rangle \rightarrow |T_\pm\rangle$ (hh) and (kk) transitions and for the $|A_0'\rangle \rightarrow |\tilde{A}_0\rangle$ (kh) transition for densities (a) $N = 1 \times 10^{15}$ cm^{-3}, (b) $N = 2 \times 10^{15}$ cm^{-3}, and (c) $N = 3 \times 10^{15}$ cm^{-3}.

using densities $N = 1 \times 10^{15}$ cm^{-3} [Fig. 9(a)], $N = 2 \times 10^{15}$ cm^{-3} [Fig. 9(b)], and $N = 3 \times 10^{15}$ cm^{-3} [Fig. 9(c)]. It is evident that the greater the density N, the more accurately the experimental curve is fitted, thus suggesting $N \gtrsim 3 \times 10^{15}$ cm^{-3}. We propose that the fluctuating charges are the nominal charges in the n region, whereas the additional charges are deeper traps due to the preparation properties of the material. These contribute to the depletion curves but do not contribute to the optical linewidths due to their deep trap status.

APPENDIX B: PHOTOLUMINESCENCE FOR ALTERNATIVE RATIOS OF TRAPPED ELECTRONS

In Fig. 10 we plot the photoluminescence of the single (kk) divacancy with $|E_y\rangle \rightarrow |T_0\rangle$ and $|E_{1,2}\rangle \rightarrow |T_\pm\rangle$ addressed transitions for different fractions of trapped electrons: namely, 1/8 [Fig. 10(a)], 3/4 [Fig. 10(b)], and 1/2 [Fig. 10(c)]. It is evident that even for different concentrations of trapped electrons, Fig. 10 still reproduces accurately the experimental data in Fig. 7(b).

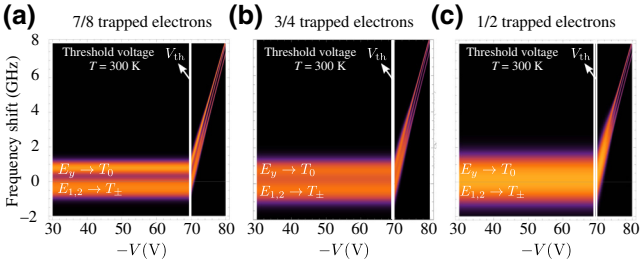

FIG. 10. Single (kk) divacancy photoluminescence with $|E_y\rangle \rightarrow |T_0\rangle$ and $|E_{1,2}\rangle \rightarrow |T_\pm\rangle$ addressed transitions for (a) 7/8, (b) 3/4, and (c) 1/2 fractions of trapped electrons.

[1] C. P. Anderson, A. Bourassa, K. C. Miao, G. Wolfowicz, P. J. Mintun, A. L. Crook, H. Abe, J. Ul Hassan, N. T. Son, T. Ohshima, and D. D. Awschalom, Electrical and optical control of single spins integrated in scalable semiconductor devices, Science **366**, 1225 (2019).

[2] N. Gisin, G. Ribordy, W. Tittel, and H. Zbinden, Quantum cryptography, Rev. Mod. Phys. **74**, 145 (2002).

[3] N. T. Son, C. P. Anderson, A. Bourassa, K. C. Miao, C. Babin, M. Widmann, M. Niethammer, J. Ul Hassan, N. Morioka, I. G. Ivanov, F. Kaiser, J. Wrachtrup, and D. D. Awschalom, Developing silicon carbide for quantum spintronics, Appl. Phys. Lett. **116**, 190501 (2020).

[4] F. Dolde *et al.*, Electric-field sensing using single diamond spins, Nat. Phys. **7**, 459 (2011).

[5] P. Jamonneau, M. Lesik, J. P. Tetienne, I. Alvizu, L. Mayer, A. Dréau, S. Kosen, J.-F. Roch, S. Pezzagna, J. Meijer, T. Teraji, Y. Kubo, P. Bertet, J. R. Maze, and V. Jacques, Competition between electric field and magnetic field noise in the decoherence of a single spin in diamond, Phys. Rev. B **93**, 024305 (2016).

[6] S. Sangtawesin, B. L. Dwyer, S. Srinivasan, J. J. Allred, L. V. H. Rodgers, K. De Greve, A. Stacey, N. Dontschuk, K. M. O'Donnell, D. Hu, D. A. Evans, C. Jaye, D. A. Fischer, M. L. Markham, D. J. Twitchen, H. Park, M. D. Lukin, and N. P. de Leon, Origins of Diamond Surface Noise Probed by Correlating Single-Spin Measurements with Surface Spectroscopy, Phys. Rev. X **9**, 031052 (2019).

[7] C. S. Shin, C. E. Avalos, M. C. Butler, H.-J. Wang, S. J. Seltzer, R.-B. Liu, A. Pines, and V. S. Bajaj, Suppression of electron spin decoherence of the diamond NV center by a transverse magnetic field, Phys. Rev. B **88**, 161412 (2013).

[8] G. Balasubramanian, P. Neumann, D. Twitchen, M. Markham, R. Kolesov, N. Mizuochi, J. Isoya, J. Achard, J. Beck, J. Tissler, V. Jacques, P. R. Hemmer, F. Jelezko, and J. Wrachtrup, Ultralong spin coherence time in isotopically engineered diamond, Nat. Mater. **8**, 383 (2009).

[9] C. A. Meriles, L. Jiang, G. Goldstein, J. S. Hodges, J. Maze, M. D. Lukin, and P. Cappellaro, Imaging mesoscopic nuclear spin noise with a diamond magnetometer, J. Chem. Phys. **133**, 124105 (2010).

[10] T. Rosskopf, A. Dussaux, K. Ohashi, M. Loretz, R. Schirhagl, H. Watanabe, S. Shikata, K. M. Itoh, and C. L. Degen, Investigation of Surface Magnetic Noise by Shallow Spins in Diamond, Phys. Rev. Lett. **112**, 147602 (2014).

[11] B. A. Myers, A. Das, M. C. Dartiailh, K. Ohno, D. D. Awschalom, and A. C. Bleszynski Jayich, Probing Surface Noise with Depth-Calibrated Spins in Diamond, Phys. Rev. Lett. **113**, 027602 (2014).

[12] Y. Romach, C. Müller, T. Unden, L. J. Rogers, T. Isoda, K. M. Itoh, M. Markham, A. Stacey, J. Meijer, S. Pezzagna, B. Naydenov, L. P. McGuinness, N. Bar-Gill, and F. Jelezko, Spectroscopy of Surface-Induced Noise Using Shallow Spins in Diamond, Phys. Rev. Lett. **114**, 017601 (2015).

[13] B. A. Myers, A. Ariyaratne, and A. C. B. Jayich, Double-Quantum Spin-Relaxation Limits to Coherence of Near-Surface Nitrogen-Vacancy Centers, Phys. Rev. Lett. **118**, 197201 (2017).

[14] J. Choi, S. Choi, G. Kucsko, P. C. Maurer, B. J. Shields, H. Sumiya, S. Onoda, J. Isoya, E. Demler, F. Jelezko, N. Y. Yao, and M. D. Lukin, Depolarization Dynamics in a Strongly Interacting Solid-State Spin Ensemble, Phys. Rev. Lett. **118**, 093601 (2017).

[15] K. C. Miao, A. Bourassa, C. P. Anderson, S. J. Whiteley, A. L. Crook, S. L. Bayliss, G. Wolfowicz, G. Thiering, P. Udvarhelyi, V. Ivády, H. Abe, T. Ohshima, Á. Gali, and D. D. Awschalom, Electrically driven optical interferometry with spins in silicon carbide, Sci. Adv. **5**, eaay0527 (2019).

[16] A. Bourassa, C. P. Anderson, K. C. Miao, M. Onizhuk, H. Ma, A. L. Crook, H. Abe, J. Ul-Hassan, T. Ohshima, N. T. Son, G. Galli, and D. D. Awschalom, Entanglement and control of single nuclear spins in isotopically engineered silicon carbide, Nat. Mater. **19**, 1319 (2020).

[17] M. Kim, H. J. Mamin, M. H. Sherwood, K. Ohno, D. D. Awschalom, and D. Rugar, Decoherence of Near-Surface Nitrogen-Vacancy Centers due to Electric Field Noise, Phys. Rev. Lett. **115**, 087602 (2015).

[18] P. Chrostoski, H. R. Sadeghpour, and D. H. Santamore, Electric Noise Spectra of a Near-Surface Nitrogen-Vacancy Center in Diamond with a Protective Layer, Phys. Rev. Appl. **10**, 064056 (2018).

[19] T. Mittiga, S. Hsieh, C. Zu, B. Kobrin, F. Machado, P. Bhattacharyya, N. Z. Rui, A. Jarmola, S. Choi, D. Budker, and N. Y. Yao, Imaging the Local Charge Environment of Nitrogen-Vacancy Centers in Diamond, Phys. Rev. Lett. **121**, 246402 (2018).

[20] B. B. Zhou, P. C. Jerger, K.-H. Lee, M. Fukami, F. Mujid, J. Park, and D. D. Awschalom, Spatiotemporal Mapping of a Photocurrent Vortex in Monolayer MoS_2 Using Diamond Quantum Sensors, Phys. Rev. X **10**, 011003 (2020).

[21] R. Schirhagl, K. Chang, M. Loretz, and C. L. Degen, Nitrogen-vacancy centers in diamond: Nanoscale sensors for physics and biology, Annu. Rev. Phys. Chem. **65**, 83 (2014).

[22] F. Dolde, M. W. Doherty, J. Michl, I. Jakobi, B. Naydenov, S. Pezzagna, J. Meijer, P. Neumann, F. Jelezko, N. B. Manson, and J. Wrachtrup, Nanoscale Detection of a Single Fundamental Charge in Ambient Conditions Using the NV^- Center in Diamond, Phys. Rev. Lett. **112**, 097603 (2014).

[23] C. L. Degen, F. Reinhard, and P. Cappellaro, Quantum sensing, Rev. Mod. Phys. **89**, 035002 (2017).

[24] G. Fuchs, G. Burkard, P. Klimov, and D. Awschalom, A quantum memory intrinsic to single nitrogen–vacancy centres in diamond, Nat. Phys. **7**, 789 (2011).

[25] B. Hensen, H. Bernien, A. E. Dréau, A. Reiserer, N. Kalb, M. S. Blok, J. Ruitenberg, R. F. L. Vermeulen, R. N. Schouten, C. Abellán, W. Amaya, V. Pruneri, M. W. Mitchell, M. Markham, D. J. Twitchen, D. Elkouss, S. Wehner, T. H. Taminiau, and R. Hanson, Loophole-free Bell inequality violation using electron spins separated by 1.3 kilometres, Nature **526**, 682 (2015).

[26] L. Robledo, L. Childress, H. Bernien, B. Hensen, P. F. Alkemade, and R. Hanson, High-fidelity projective read-out of a solid-state spin quantum register, Nature **477**, 574 (2011).

[27] D. D. Awschalom, R. Hanson, J. Wrachtrup, and B. B. Zhou, Quantum technologies with optically interfaced solid-state spins, Nat. Photonics **12**, 516 (2018).

[28] E. Togan, Y. Chu, A. S. Trifonov, L. Jiang, J. Maze, L. Childress, M. V. G. Dutt, A. S. Sørensen, P. R. Hemmer, A. S. Zibrov, and M. D. Lukin, Quantum entanglement between an optical photon and a solid-state spin qubit, Nature **466**, 730 (2010).

[29] G. de Lange, Z. H. Wang, D. Ristè, V. V. Dobrovitski, and R. Hanson, Universal dynamical decoupling of a single solid-state spin from a spin bath, Science **330**, 60 (2010).

[30] S. Wehner, D. Elkouss, and R. Hanson, Quantum internet: A vision for the road ahead, Science **362**, eaam9288 (2018).

[31] L. Trifunovic, F. L. Pedrocchi, and D. Loss, Long-Distance Entanglement of Spin Qubits via Ferromagnet, Phys. Rev. X **3**, 041023 (2013).

[32] P. Andrich, C. F. de las Casas, X. Liu, H. L. Bretscher, J. R. Berman, F. J. Heremans, P. F. Nealey, and D. D. Awschalom, Long-range spin wave mediated control of defect qubits in nanodiamonds, npj Quantum Inf **3**, 28 (2017).

[33] Y.-Y. Lai, G.-D. Lin, J. Twamley, and H.-S. Goan, Single-nitrogen-vacancy-center quantum memory for a superconducting flux qubit mediated by a ferromagnet, Phys. Rev. A **97**, 052303 (2018).

[34] C. Mühlherr, V. O. Shkolnikov, and G. Burkard, Magnetic resonance in defect spins mediated by spin waves, Phys. Rev. B **99**, 195413 (2019).

[35] B. Flebus and Y. Tserkovnyak, Entangling distant spin qubits via a magnetic domain wall, Phys. Rev. B **99**, 140403 (2019).

[36] E. Lee-Wong, R. Xue, F. Ye, A. Kreisel, T. van der Sar, A. Yacoby, and C. R. Du, Nanoscale detection of magnon excitations with variable wavevectors through a quantum spin sensor, Nano Lett. **20**, 3284 (2020).

[37] D. R. Candido, G. D. Fuchs, E. Johnston-Halperin, and M. E. Flatté, Predicted strong coupling of solid-state spins via a single magnon mode, Mat. Quantum Technol. **1**, 011001 (2021).

[38] T. Neuman, D. S. Wang, and P. Narang, Nanomagnonic Cavities for Strong Spin-Magnon Coupling and Magnon-Mediated Spin-Spin Interactions, Phys. Rev. Lett. **125**, 247702 (2020).

[39] J. Zou, S. K. Kim, and Y. Tserkovnyak, Tuning entanglement by squeezing magnons in anisotropic magnets, Phys. Rev. B **101**, 014416 (2020).

[40] M. Fukami, D. R. Candido, D. D. Awschalom, and M. E. Flatté, Opportunities for long-range magnon-mediated entanglement of spin qubits via on-and off-resonant coupling, PRX Quantum (in press).

[41] J. Lowther, Vacancies and divacancies in cubic silicon carbide, J. Phys. C: Solid State Phys. **10**, 2501 (1977).

[42] A. L. Falk, P. V. Klimov, B. B. Buckley, V. Ivády, I. A. Abrikosov, G. Calusine, W. F. Koehl, A. Gali, and D. D. Awschalom, Optical Polarization of Nuclear Spins in Silicon Carbide, Phys. Rev. Lett. **112**, 187601 (2014).

[43] H. Seo, A. L. Falk, P. V. Klimov, K. C. Miao, G. Galli, and D. D. Awschalom, Quantum decoherence dynamics of divacancy spins in silicon carbide, Nat. Commun. **7**, 12935 (2016).

[44] C. F. de las Casas, D. J. Christle, J. Ul Hassan, T. Ohshima, N. T. Son, and D. D. Awschalom, Stark tuning and electrical

charge state control of single divacancies in silicon carbide, Appl. Phys. Lett. **111**, 262403 (2017).

[45] V. Ivády, K. Szász, A. L. Falk, P. V. Klimov, D. J. Christle, E. Janzén, I. A. Abrikosov, D. D. Awschalom, and A. Gali, Theoretical model of dynamic spin polarization of nuclei coupled to paramagnetic point defects in diamond and silicon carbide, Phys. Rev. B **92**, 115206 (2015).

[46] M. W. Doherty, N. B. Manson, P. Delaney, F. Jelezko, J. Wrachtrup, and L. C. L. Hollenberg, The nitrogen-vacancy colour centre in diamond, Phys. Rep. **528**, 1 (2013).

[47] F. Casola, T. van der Sar, and A. Yacoby, Probing condensed matter physics with magnetometry based on nitrogen-vacancy centres in diamond, Nat. Rev. Mater. **3**, 17088 (2018).

[48] A. L. Crook, C. P. Anderson, K. C. Miao, A. Bourassa, H. Lee, S. L. Bayliss, D. O. Bracher, X. Zhang, H. Abe, T. Ohshima, E. L. Hu, and D. D. Awschalom, Purcell enhancement of a single silicon carbide color center with coherent spin control, Nano Lett. **20**, 3427 (2020).

[49] D. Y. Fedyanin and M. Agio, Ultrabright single-photon source on diamond with electrical pumping at room and high temperatures, New J. Phys. **18**, 073012 (2016).

[50] I. A. Khramtsov, M. Agio, and D. Y. Fedyanin, Dynamics of Single-Photon Emission from Electrically Pumped Color Centers, Phys. Rev. Appl. **8**, 024031 (2017).

[51] I. A. Khramtsov, A. A. Vyshnevyy, and D. Y. Fedyanin, Enhancing the brightness of electrically driven single-photon sources using color centers in silicon carbide, npj Quantum Inf **4**, 15 (2018).

[52] M. Widmann, M. Niethammer, T. Makino, T. Rendler, S. Lasse, T. Ohshima, J. Ul Hassan, N. Tien Son, S.-Y. Lee, and J. Wrachtrup, Bright single photon sources in lateral silicon carbide light emitting diodes, Appl. Phys. Lett. **112**, 231103 (2018).

[53] I. A. Khramtsov and D. Y. Fedyanin, Toward ultrafast tuning and triggering single-photon electroluminescence of color centers in silicon carbide, ACS Appl. Electron. Mater. **1**, 1859 (2019).

[54] M. Widmann, M. Niethammer, D. Y. Fedyanin, I. A. Khramtsov, T. Rendler, I. D. Booker, J. Ul Hassan, N. Morioka, Y.-C. Chen, I. G. Ivanov, N. T. Son, T. Ohshima, M. Bockstedte, A. Gali, C. Bonato, S.-Y. Lee, and J. Wrachtrup, Electrical charge state manipulation of single silicon vacancies in a silicon carbide quantum optoelectronic device, Nano Lett. **19**, 7173 (2019).

[55] P. Tamarat, T. Gaebel, J. R. Rabeau, M. Khan, A. D. Greentree, H. Wilson, L. C. L. Hollenberg, S. Prawer, P. Hemmer, F. Jelezko, and J. Wrachtrup, Stark Shift Control of Single Optical Centers in Diamond, Phys. Rev. Lett. **97**, 083002 (2006).

[56] L. C. Bassett, F. J. Heremans, C. G. Yale, B. B. Buckley, and D. D. Awschalom, Electrical Tuning of Single Nitrogen-Vacancy Center Optical Transitions Enhanced by Photoinduced Fields, Phys. Rev. Lett. **107**, 266403 (2011).

[57] V. M. Acosta, C. Santori, A. Faraon, Z. Huang, K.-M. C. Fu, A. Stacey, D. A. Simpson, K. Ganesan, S. Tomljenovic-Hanic, A. D. Greentree, S. Prawer, and R. G. Beausoleil, Dynamic Stabilization of the Optical Resonances of Single Nitrogen-Vacancy Centers in Diamond, Phys. Rev. Lett. **108**, 206401 (2012).

[58] P. V. Klimov, A. L. Falk, B. B. Buckley, and D. D. Awschalom, Electrically Driven Spin Resonance in Silicon Carbide Color Centers, Phys. Rev. Lett. **112**, 087601 (2014).

[59] D. J. Christle, P. V. Klimov, C. F. de las Casas, K. Szász, V. Ivády, V. Jokubavicius, J. Ul Hassan, M. Syväjärvi, W. F. Koehl, T. Ohshima, N. T. Son, E. Janzén, A. Gali, and D. D. Awschalom, Isolated Spin Qubits in SiC with a High-Fidelity Infrared Spin-To-Photon Interface, Phys. Rev. X **7**, 021046 (2017).

[60] A. M. Stoneham, *Theory of Defects in Solids* (Oxford University Press, Oxford, UK, 2001).

[61] A. Kiel and W. B. Mims, Linear electric field effect in paramagnetic resonance for CdS: Mn^{2+}, Phys. Rev. B **5**, 803 (1972).

[62] J. H. N. Loubser and J. A. van Wyk, Electron spin resonance in the study of diamond, Rep. Prog. Phys. **41**, 1201 (1978).

[63] E. Van Oort and M. Glasbeek, Electric-field-induced modulation of spin echoes of N-V centers in diamond, Chem. Phys. Lett. **168**, 529 (1990).

[64] F. M. Hossain, M. W. Doherty, H. F. Wilson, and L. C. L. Hollenberg, *Ab Initio* Electronic and Optical Properties of the $N\text{-}V^-$ Center in Diamond, Phys. Rev. Lett. **101**, 226403 (2008).

[65] J. R. Maze, A. Gali, E. Togan, Y. Chu, A. Trifonov, E. Kaxiras, and M. D. Lukin, Properties of nitrogen-vacancy centers in diamond: The group theoretic approach, New J. Phys. **13**, 025025 (2011).

[66] M. W. Doherty, N. B. Manson, P. Delaney, and L. C. L. Hollenberg, The negatively charged nitrogen-vacancy centre in diamond: The electronic solution, New J. Phys. **13**, 025019 (2011).

[67] M. W. Doherty, F. Dolde, H. Fedder, F. Jelezko, J. Wrachtrup, N. B. Manson, and L. C. L. Hollenberg, Theory of the ground-state spin of the NV^- center in diamond, Phys. Rev. B **85**, 205203 (2012).

[68] L. J. Rogers, M. W. Doherty, M. S. J. Barson, S. Onoda, T. Ohshima, and N. B. Manson, Singlet levels of the NV-centre in diamond, New J. Phys. **17**, 013048 (2015).

[69] P. Udvarhelyi, V. O. Shkolnikov, A. Gali, G. Burkard, and A. Pályi, Spin-strain interaction in nitrogen-vacancy centers in diamond, Phys. Rev. B **98**, 075201 (2018).

[70] H. Y. Chen, S. A. Bhave, and G. D. Fuchs, Acoustically Driving the Single-Quantum Spin Transition of Diamond Nitrogen-Vacancy Centers, Phys. Rev. Appl. **13**, 054068 (2020).

[71] A. Jarmola, V. M. Acosta, K. Jensen, S. Chemerisov, and D. Budker, Temperature- and Magnetic-Field-Dependent Longitudinal Spin Relaxation in Nitrogen-Vacancy Ensembles in Diamond, Phys. Rev. Lett. **108**, 197601 (2012).

[72] H.-J. Wang, C. S. Shin, C. E. Avalos, S. J. Seltzer, D. Budker, A. Pines, and V. S. Bajaj, Sensitive magnetic control of ensemble nuclear spin hyperpolarization in diamond, Nat. Commun. **4**, 1940 (2013).

[73] A. L. Falk, P. V. Klimov, V. Ivády, K. Szász, D. J. Christle, W. F. Koehl, A. Gali, and D. D. Awschalom, Optical Polarization of Nuclear Spins in Silicon Carbide, Phys. Rev. Lett. **114**, 247603 (2015).

[74] A. Wickenbrock, H. Zheng, L. Bougas, N. Leefer, S. Afach, A. Jarmola, V. M. Acosta, and D. Budker, Microwave-free magnetometry with nitrogen-vacancy centers in diamond, Appl. Phys. Lett. **109**, 053505 (2016).

[75] D. A. Broadway, J. D. A. Wood, L. T. Hall, A. Stacey, M. Markham, D. A. Simpson, J.-P. Tetienne, and L. C. L. Hollenberg, Anticrossing Spin Dynamics of Diamond Nitrogen-Vacancy Centers and All-Optical Low-Frequency Magnetometry, Phys. Rev. Appl. **6**, 064001 (2016).

[76] S. A. Tarasenko, A. V. Poshakinskiy, D. Simin, V. A. Soltamov, E. N. Mokhov, P. G. Baranov, V. Dyakonov, and G. V. Astakhov, Spin and optical properties of silicon vacancies in silicon carbide – a review, Phys. Status Solidi (b) **255**, 1700258 (2018).

[77] M. Auzinsh, A. Berzins, D. Budker, L. Busaite, R. Ferber, F. Gahbauer, R. Lazda, A. Wickenbrock, and H. Zheng, Hyperfine level structure in nitrogen-vacancy centers near the ground-state level anticrossing, Phys. Rev. B **100**, 075204 (2019).

[78] L. Busaite, R. Lazda, A. Berzins, M. Auzinsh, R. Ferber, and F. Gahbauer, Dynamic ^{14}N nuclear spin polarization in nitrogen-vacancy centers in diamond, Phys. Rev. B **102**, 224101 (2020).

[79] H. Zheng, Z. Sun, G. Chatzidrosos, C. Zhang, K. Nakamura, H. Sumiya, T. Ohshima, J. Isoya, J. Wrachtrup, A. Wickenbrock, and D. Budker, Microwave-Free Vector Magnetometry with Nitrogen-Vacancy Centers along a Single Axis in Diamond, Phys. Rev. Appl. **13**, 044023 (2020).

[80] V. Ivády, H. Zheng, A. Wickenbrock, L. Bougas, G. Chatzidrosos, K. Nakamura, H. Sumiya, T. Ohshima, J. Isoya, D. Budker, I. A. Abrikosov, and A. Gali, Photoluminescence at the ground-state level anticrossing of the nitrogen-vacancy center in diamond: A comprehensive study, Phys. Rev. B **103**, 035307 (2021).

[81] C. P. Anderson, PhD thesis, The University of Chicago, 2020, https://knowledge.uchicago.edu/record/2263.

[82] P. W. Anderson and P. R. Weiss, Exchange narrowing in paramagnetic resonance, Rev. Mod. Phys. **25**, 269 (1953).

[83] H. Iwata, K. M. Itoh, and G. Pensl, Theory of the anisotropy of the electron hall mobility in *n*-type 4H– and 6H-SiC, J. Appl. Phys. **88**, 1956 (2000).

[84] Because of the lack of experimental data for (hh) and (kk) divacancy ground-state dipoles, here we use the dipole values corresponding to the (hk) and (kh) divacancies [42].